Finding and identifying simple objects underwater with active electrosense

Yang Bai[1], James B. Snyder[2], Michael Peshkin[1] and Malcolm A. MacIver[1,2,3]

Abstract
Active electrosense is used by some fish for the sensing of nearby objects by means of the perturbations the objects induce in a self-generated electric field. As with echolocation (sensing via perturbations of an emitted acoustic field) active electrosense is particularly useful in environments where darkness, clutter or turbidity makes vision ineffective. Work on engineered variants of active electrosense is motivated by the need for sensors in underwater systems that function well at short range and where vision-based approaches can be problematic, as well as to aid in understanding the computational principles of biological active electrosense. Prior work in robotic active electrosense has focused on tracking and localization of spherical objects. In this study, we present an algorithm for estimating the size, shape, orientation, and location of ellipsoidal objects, along with experimental results. The algorithm is implemented in a robotic active electrosense system whose basic approach is similar to biological active electrosense systems, including the use of movement as part of sensing. At a range up to ≈20 cm, or about half the length of the robot, the algorithm localizes spheroids that are one-tenth the length of the robot with accuracy of better than 1 cm for position and 5° in orientation. The algorithm estimates object size and length-to-width ratio with an accuracy of around 10%.

Keywords
Artificial electrosense, active sensing, object identification

1. Introduction

Electrosense is one of the most recently discovered sensory modalities, having been discovered in a freshwater African fish in the mid-20th century (Lissmann and Machin, 1958). While many fish, including catfish and sharks, are able to detect electrical fields that originate from outside of their body, only two groups of freshwater "weakly electric" fish both emit and detect an electric field as an active sensing system similar to sonar or radar. These biological "active electrolocators" have been the subject of intense investigation (reviews: Turner et al., 1999; Krahe and Fortune, 2013).

Prior work has examined the relationship between the pattern of electric field perturbations on the surface of a fish (the "electric image") and the properties of the object causing those perturbations. Behavioral studies have provided some clues about how features of the detected signal can be used to localize and identify an external object (Assad et al., 1999; Nelson and MacIver, 1999; Von der Emde, 2006), and fish have been trained to discriminate objects based on their geometric properties and composition (Lissmann and Machin, 1958; Von der Emde and Fetz, 2007). Studies have also shown relationships between simple object (spheres) properties and electric image features

(Rasnow, 1996; Assad et al., 1999). For example, given the electric field of the fish, the location of a spherical object is related to the location of the peak amplitude of the electric image on the fish body.

The work on biological electrosense has inspired work on engineered variants of electrosense, including voltage sensing approaches (Solberg et al., 2008; Nguyen et al., 2009; Bai et al., 2012; Silverman et al., 2012; Snyder et al., 2012; Neveln et al., 2013; Dimble et al., 2014) and current sensing approaches (Baffet et al., 2009; Boyer et al., 2012; Lebastard et al., 2013; Servagent et al., 2013). Active electrosense systems complement existing technologies, such as acoustic and visual sensing (Cowen et al., 1997; Smith

[1]Department of Mechanical Engineering, Northwestern University, Evanston, IL, USA
[2]Department of Biomedical Engineering, Northwestern University, Evanston, IL, USA
[3]Department of Neurobiology, Northwestern University, Evanston, IL, USA

Corresponding author:
Malcolm A MacIver, Northwestern University, 2145 Sheridan Road, Tech B224, Evanston, IL, 60208 USA.
Email: maciver@northwestern.edu

et al., 1999; Jaffré et al., 2005; Singh et al., 2007; Yoerger et al., 2007; Hollinger et al., 2013), and address the need for better short range sensors for cluttered and turbid underwater conditions (MacIver et al., 2004), such as the Deepwater Horizon disaster (Kinsey et al., 2011). Active electrosense works well in confined spaces where sonar can suffer from multipath reflections that can make interpretation of signals difficult when the sensor is near to boundaries (Pinto et al., 2004; Davis et al., 2009). Work on this approach also furthers our understanding of the fundamental mechanisms used by the electric fish, which is a leading model system within neuroscience for understanding the mechanisms of sensory signal processing in animals.

Solving the localization and reconstruction problem through the electric images of arbitrary objects and environments is quite difficult. Spheroids, obtained by revolving an ellipse around one of its two axes, approximate the shape of a large number of objects while still being analytically tractable (Shiau and Valentino, 1981; Valič et al., 2003). However, the complexity of a spheroid's electric image prohibits the use of simple analytical models for localization and shape estimation, as is possible for spheres (Landau and Lifshitz, 1984; Rasnow, 1996). The difficulty of geometric property reconstruction is exacerbated by the non-uniformity of realistic electric fields, the distortion of which is even larger with spheroids than spheres. Statistical learning techniques, widely applied in 3D reconstruction in machine vision systems (Hornegger and Niemann, 1995), allow the construction of non-linear models to estimate geometric parameters related to the external object (Alamir et al., 2010). Specifically, a supervised learning model, trained from measurement data, readily takes into account the complex, non-linear properties of the object and the electric field. In addition, instead of using a single sensor, we take advantage of using a sensor array to gain more information for object localization and reconstruction.

In this study, we focus on the design and testing of active motion and statistical learning algorithms to localize and reconstruct prolate spheroids. Prolate spheroids are generated by revolution around the long axis of an ellipse, while oblate spheroids are generated by revolution around the short axis. As the electric images of prolate and oblate spheroids are quite similar, we focus on prolate spheroids and show that our approach can be extended to oblate spheroids.

Our robotic electrolocator (hereafter "SensorPod") consists of two excitation electrodes and multiple pairs of differential sensing electrodes. Figure 1 shows simulations of isopotentials around the SensorPod, illustrating how these are distorted by spheroids of different shapes, orientations, and conductivity. We show these distortions in the horizontal plane that bisects the SensorPod into top and bottom halves. Below those images we illustrate how the potential sensed by the differential sensing electrodes at the surface of the SensorPod vary as a result of the presence of the corresponding object. The specific pattern of voltages along the sensors for each object is that object's electric image.

Each differential pair of sensors registers the difference between the left side and right side of the SensorPod (we designate the $+10$ V side as the front). The electric field is non-uniform in both direction and magnitude.

1.1. Previous work and contribution

Our work is motivated by previous work in underwater artificial electrosense and active motion commonly used in other active sensing modalities. Artificial active electrosense systems have been used, like other sensing modalities (Szeliski and Kang, 1995; Sequeira et al., 1999; Coiras et al., 2007; Fairfield et al., 2010), for one generic task, the reconstruction of objects in the environment. Of specific interest is the reconstruction of geometric parameters. Normally, given the parameters, the computation of the sensory data, the electric image in our case, involves solving Laplace's equation with boundary conditions. However, estimating object properties from the electric images, the inverse problem, is called the Calderón problem (Calderón, 2006) and is typically severely ill-posed (Dines and Lytle, 1981).

Using a variant of electric impedance tomography (EIT), Snyder et al. (2012) relied on altering the electric field configuration and reconstructed the environment in resistivity mapping in simulation. This approach could potentially be extended to impedance mapping (Cheney et al., 1999; Church et al., 2006). In another recent simulation study, Ammari et al. (2013, 2014) used multi-frequency measurements and a complex forward model to search through position space to localize a capacitive object. Size and composition were later derived with model fitting. This work also presented a dictionary-based shape classifier. In both simulation studies, the sensing device remains stationary and significant computation is used to solve the inverse problem directly.

Motion or active sensing, commonly used in both biological and engineered visual and acoustic sensory systems for localization and navigation (Fox et al., 1998; Feder et al., 1999; Kreucher et al., 2005; Weingarten and Siegwart, 2005; Nelson and MacIver, 2006; Sattar et al., 2009; Webster et al., 2012), provides an alternative to solving the inverse problem directly. Instead of being stationary, sensing devices explore the surroundings to reconstruct part of the environment of interest. Some studies in electric field sensing have already demonstrated simple active exploration abilities such as wall-following (Baffet et al., 2009; Jawad et al., 2010; Boyer and Lebastard, 2012; Boyer et al., 2013) and object avoidance (Boyer et al., 2013; Dimble et al., 2014). In the context of probabilistic robotics, Solberg et al. applied a particle filter and a dipole model to actively localize a sphere underwater (Solberg et al., 2008). Boyer et al. used various state space filtering techniques and measurement models to actively reconstruct the position and size of small spheres and cubes (Lebastard et al., 2010; Boyer et al., 2012; Lebastard et al., 2013; Servagent et al., 2013). To optimize active sensing, metrics
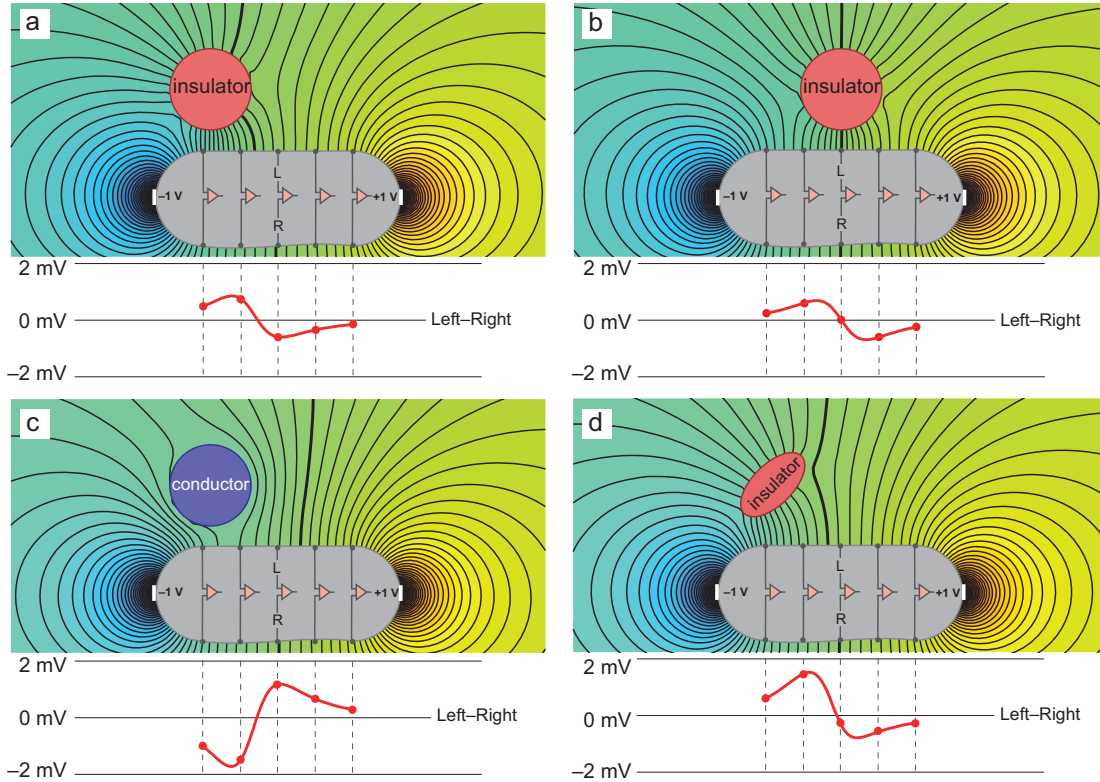
Fig. 1. Electric images from a 3D simulation of our robotic electrolocator ("SensorPod", shown in a view from above, pill-shaped in gray). The two excitation electrodes in white at each end of the SensorPod generate a symmetric AC electric field. The two AC signals at both ends are 180° out of phase and 1 V amplitude (in experiments the real SensorPod used 10 V amplitude). Because the signals are always opposite in sign, we denote them as $+1$ V and -1 V. We designate the $+1$ V end as the front of the SensorPod. The isopotential lines are drawn in black with the 0 V isopotential line in bold. Five pairs of differential sensing electrodes in gray measure the perturbation caused by an external object. Voltage profiles are given for three different scenarios: (a) a spherical insulator, positioned to the left and behind the center of the SensorPod; (b) a spherical insulator, positioned to the left and midway down the SensorPod; (c) a spherical conductor, in the same position as the object in (a); (d) a non-conductive prolate spheroid, in the same position as the object in (a). The electric image of a non-conductive sphere (a) is half the magnitude of a conductive sphere (c) and opposite in sign. Movies showing the evolution of the electric image as distance, position, shape and size of target varies can be found in Multimedia Extension 1 (see the appendix).

of information (Frieden, 2004; Cover and Thomas, 2012) are incorporated to obtain the optimal motion for sensory data acquisition (Takeuchi et al., 1998; Li and Liu, 2005; Hollinger et al., 2013) and have been applied in electric field sensing (Silverman et al., 2013). The above active electric sensing approaches focus on the reconstruction of the position of a simple object which is spherical or near-spherical.

In visual and acoustic systems, it is advantageous to employ sensor arrays to obtain wider coverage (Horster and Lienhart, 2006) and high reconstruction precision (Araujo and Grupen, 1998). Except for a multiple current sensor configuration in the work of Boyer's group (see Servagent et al., 2013), most of the previously mentioned robotic electrosense systems use a single voltage sensor, a major difference from the electric fish as mentioned above. The synthesis of a sensor array with motion has not been explored in engineered active electrosense devices.

When dealing with complex spheroid scenarios, our approach combines the merits of active sensing, statistical

learning, and sensor array processing. Our SensorPod actively explores the environment to arrive at a near-optimal position for the sensor array (based on Fisher information) and then uses statistical learning techniques to tackle the non-linearity induced by the non-uniform electric field and spheroid geometry.

1.2. Algorithm overview

The algorithm consists of two stages: active alignment and identification. Both stages exploit the symmetry of both the SensorPod and spheroids to transform a difficult non-linear identification problem into a sequential series of parameter estimations.

In the active alignment stage, the goal of the SensorPod is to align with the object in order to obtain a symmetric electric image. Specifically, at the end of this stage, the object is lateral to the robot and midway down its length (Figure 1(b)). When the SensorPod is aligned with the object in this way, orientation and longitudinal position is
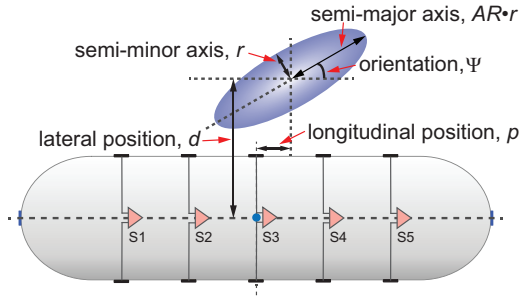
Fig. 2. Definition of parameters estimated by the algorithm. The shape of a prolate spheroid is defined by its semi-minor axis r and aspect ratio AR. Orientation Ψ is the relative angular difference between the major axes of the object and SensorPod (shown in top view). After the end of the active alignment stage of the algorithm, the longitudinal position and orientation angle is zero. Note that d in this study is to the center of the SensorPod. The distance to the surface is $d - 7.62$ cm.

resolved, significantly reducing the difficulty of shape, size, and distance estimation. In addition, active alignment gives the subsequent identification stage of the algorithm a good starting point in positioning the target where the electric field has a high level of symmetry and uniformity. The identification stage handles non-linearities of the electric field and the mapping between object properties and electric images with a supervised learning model that already takes into account the non-linearity of the electric field. The learned model is built with simulation data of spheres but generalized to estimate a variety of spheroids as well.

We provide concrete examples to build intuition, starting with the simple case of a sphere. In this case, there are three geometric properties to estimate: the radius r, and the longitudinal and lateral positions p and d. Taking advantage of the symmetry of the electric field and the sphere geometry, we can move the SensorPod to a specific location as in Figure 1(b) where $p = 0$ and the electric image is symmetric. The motion reduces the complexity of the problem and the disambiguation of r and d can be readily accomplished with a supervised learning model. To do this, we use a Gaussian process regression (GPR) model to disambiguate d and r.

For the more complex case of a prolate spheroid, we estimate five parameters: the longitudinal position p, lateral position or distance d, orientation Ψ, aspect ratio AR, and semi-minor axis r, as shown in Figure 2. The two-stage sequential parameter estimation approach is shown in Figure 3. During active alignment, we use unidirectional translations and rotations to align the SensorPod with the object, thus obtaining orientation Ψ and longitudinal position p. Again, the SensorPod achieves a symmetric pose where a symmetric electric image is available. The aspect ratio AR is derived after alignment when the relative orientation is known. The second stage discounts the effect of AR and uses the same model built for spheres to estimate the lateral position d and semi-minor axis r.

The algorithm works for both conductive and non-conductive spheroids. To distinguish between conductive

and non-conductive spheroids, we simply perform a single-ended measurement to tell which side of the SensorPod the object is on. Then the polarity of the electric image (for example, compare Figure 1(a) and (c)) reveals whether the object is a conductor or an insulator. However, for economy of exposition we focus on the non-conductive spheroid case and refer to modifications needed for conductive spheroids where necessary.

The algorithm works based on the following assumptions: (1) the major axis of the spheroid is within the same plane as the electric image sensors and two electric field generation electrodes (Figure 1 shows a top view of this plane for our particular active electrosense system). This assumption is made because we only use a planar ring of 10 sensors (compared to $\approx$14,000 scattered over the surface of a typical biological electrolocator; see Carr et al., 1982). Modified versions of this algorithm could potentially work for a more general 3D estimation task with additional sensory information. (2) The object is already within range, but not on a collision course with the mobile sensor platform. We make this assumption because electrosense-based search and object avoidance algorithms are available and applicable (Solberg et al., 2008; Boyer et al., 2013; Silverman et al., 2013).

2. Overview

Section 3 ('Principle') describes the different stages of the algorithm shown in Figure 3: active alignment; aspect ratio estimation; and finally lateral position (distance) and semi-minor axis identification. With aspect ratio and semi-minor axis length known, we can then compute the major axis length and volume of the spheroid. Section 4 ('Model generation') provides details regarding the generation of models needed for the algorithm. The data for those models were generated using finite element method (FEM) simulations of the robot and test objects. Section 5 ('Implementation') describes the experimental platform used to validate the algorithm. Section 6 ('Results') presents both simulation and experimental data for active alignment and identification. In Section 7 ('Discussion'), we begin with some general remarks about the relationship between spheroid features and their corresponding electric images. We revisit and further detail the importance of motion for the algorithm, as well as various aspects of each stage of the algorithm such as sensitivity to noise and extensions for increasing the scope of the algorithm to include additional target geometries and compositions.

3. Principle

3.1. Active alignment

Figure 3 illustrates the active alignment procedure for prolate spheroids with orientation angles from $0°$ to $90°$. By exploiting symmetry, we extend the procedure to

1   *i* iteration

V_{S3}

When the object is within range of detection translate pod until $V_{S3} = 0$

Calculate symmetry ratio η_i

$$\eta_i = \sqrt{\frac{V_{s1}^{i\,2} + V_{s2}^{i\,2}}{V_{s4}^{i\,2} + V_{s5}^{i\,2}}} \quad \text{Insulator} \qquad \eta_i = \sqrt{\frac{V_{s4}^{i\,2} + V_{s5}^{i\,2}}{V_{s1}^{i\,2} + V_{s2}^{i\,2}}} \quad \text{Conductor}$$

$\eta_i > 0.90$?

YES

NO

2 i^{th} iteration

Rotate pod by $\beta_i = 0.67\theta_i$, where θ_i is an estimation of actual orientation of object Ψ_i

3 N^{th} iteration

Pod and object are now aligned
The electric image is $[V_{S1}\ V_{S2}\ V_{S3}\ V_{S4}\ V_{S5}]$

4   Rotate pod by a known angle of 45°

5   Translate pod until $V_{S3} = 0$, calculate symmetry ratio η_{AR}

$\eta_{AR} \geq 1$

$\eta_{AR} < 1$

6   Identify aspect ratio at 45°

Aspect Ratio

— Conductor
--- Insulator

Symmetry Ratio at 45° η_{AR}

7   Identify lateral position and size with alignment electric image

V_{S1} V_{S2}

d

Scale electric image by $\mathscr{F}(AR)$ r

$\mathscr{F}(AR)$

— Conductor
--- Insulator

Aspect Ratio

Fit a hypothetical sphere to scaled electric image

d

r

$(d, r) = \text{Gaussian\_Process\_Regression}(V_{s1} \cdot \mathscr{F}(AR)\ V_{s2} \cdot \mathscr{F}(AR))$
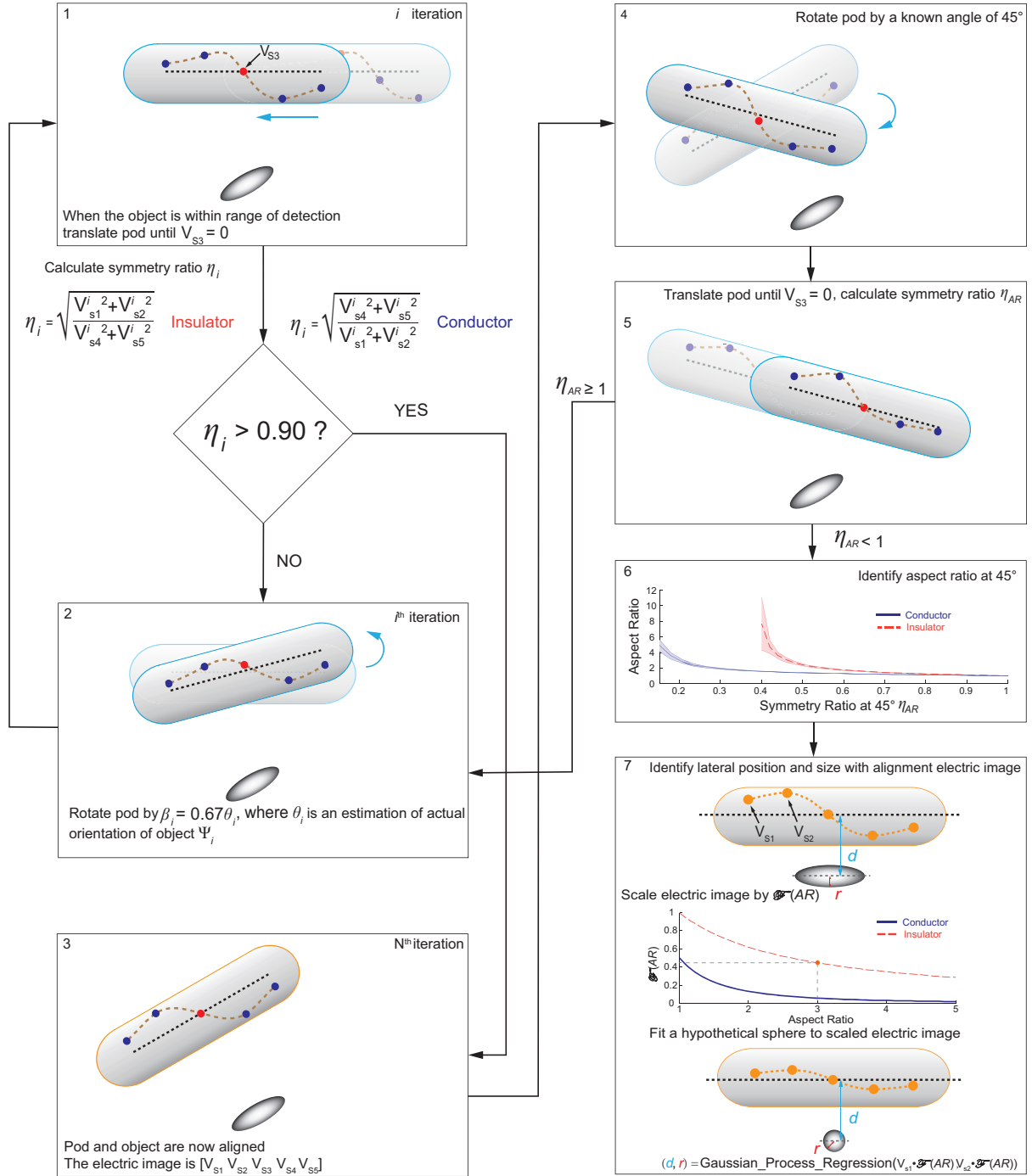
Fig. 3. Algorithm stages. On the left, alignment (longitudinal position $p = 0$, orientation $\Psi = 0$) is achieved through movement. (1) The SensorPod translates along its major axis until the middle sensor pair differential voltage is zero ($V_{S3} = 0$). If the symmetry ratio calculated is larger than a set threshold (0.90), then alignment is considered achieved. The choice of 0.90 can be seen from Figure 5. (2) Otherwise, an estimation of orientation (Ψ) is calculated to be θ, and the SensorPod rotates an angle $\beta\left(= \frac{2}{3}\theta\right)$. Now the differential voltage at the middle sensor pair is not zero. (3) After iterating through steps 1 and 2, alignment is achieved. (4),(5) After alignment, the robot rotates $45°$ and seeks the new zero-crossing where the symmetry ratio η_{AR} is calculated. (6) The aspect ratio AR is then estimated by use of a function (Figure 5) that returns aspect ratio based on η_{AR}. The shaded regions show the uncertainty of aspect ratio estimation given average uncertainty in symmetry ratio estimation in experiments. (7) To disambiguate the semi-minor axis r and lateral position d, the snapshot at alignment is first scaled by a function of the aspect ratio. Then r and p are estimated by fitting a hypothetical sphere to the scaled electric image using a GPR model for insulating spheres.
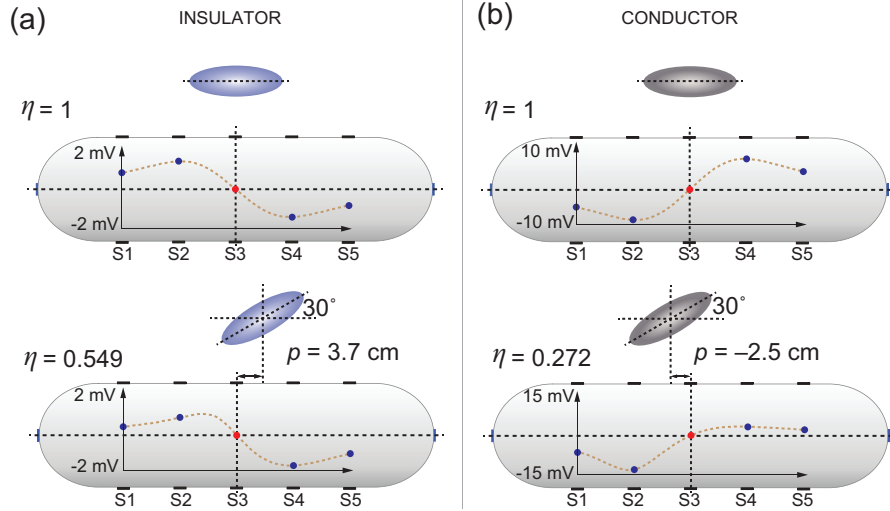
Fig. 4. Zero-crossing snapshots for different prolate spheroid poses. (a) Non-conductive prolate spheroids of different poses at zero-crossing. The symmetry ratio is unity when the prolate spheroid is aligned with the SensorPod. (b) Conductive prolate spheroids of different poses at zero-crossing. For the bottom two cases with $\Psi = 30°$ and $d = 15$ cm, the longitudinal position p at zero-crossing is different in sign and value for conductive and non-conductive prolate spheroids.

orientation angles from $0°$ to $360°$. We also cover the minor modification needed to align conductive prolate spheroids.

Alignment of prolate spheroids requires both translation and rotation (Figure 3 (1) to (3)), in contrast to spheres which can be aligned with either motion. The goal of active alignment is to move until the orientation and position is zero ($\Psi = 0°$ and $p = 0$), as shown in the first row of Figure 4.

For electric images, we define the "zero-crossing position" as the location in which the voltage at the middle sensor pair (V_{S3}) transits from positive to negative, or vice versa. Four examples of zero-crossings are shown in Figure 4. The purpose of translation during active alignment is to seek the zero-crossing position.

Once the robot is located at the zero-crossing, we compute a measure of the symmetry of the electric image. The root mean square (RMS) values of the voltages at sensors S1 and S2 are computed, and divided by the RMS of the voltages at sensors S4 and S5. We call this the "symmetry ratio" (η). For symmetric objects like prolate spheroids, when symmetry ratios are calculated and plotted against different orientations, a "symmetry map" is created, as shown in Figure 5. This map allows us to convert the symmetry ratio to an estimate of the orientation of the spheroid.

The SensorPod rotates by an angle that is smaller than the current orientation angle relative to the object so as not to overshoot. In the symmetry map, we use the outermost curve ($AR = 5$) to estimate actual orientation Ψ as θ. One symmetry ratio value usually corresponds to two orientation angles. For example, a symmetry ratio of 0.46 in Figure 5 could yield $45°$ (blue dot) and $19°$ (purple dot) if the $AR = 3$ curve is used. We use the smaller angle estimate and the SensorPod seeks to decrease the orientation

to $0°$. We further multiply by a coefficient smaller than 1, for example $\frac{2}{3}$, so that β is an underestimation of Ψ.

Translation and rotation are done separately and iteratively. We provide convincing evidence that active alignment converges (Figure 3 (3)) for a great number of cases (supplementary material, Section 2). A definitive proof based on control theory could be achieved in the future. It is possible that the first estimate of the symmetry ratio passes a set threshold (0.90). In that case, the object is considered aligned (Figure 3 (3)). Otherwise, an estimate of the orientation Ψ is calculated by referring to the symmetry
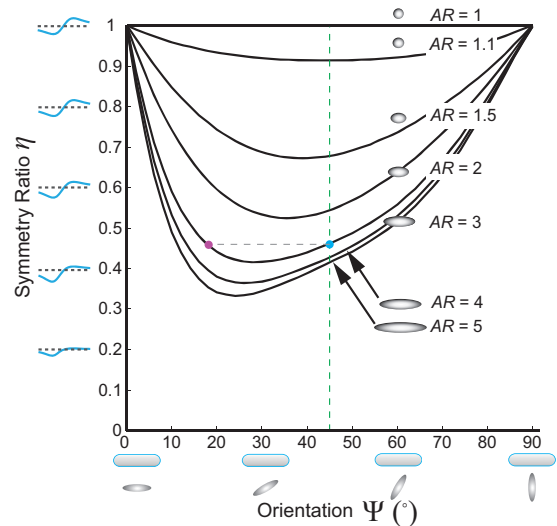

Fig. 5. The relationship between orientation Ψ and symmetry ratio η for different aspect ratios. The aspect ratio of the prolate spheroid is determined at $\Psi = 45°$ shown as the dashed green line.
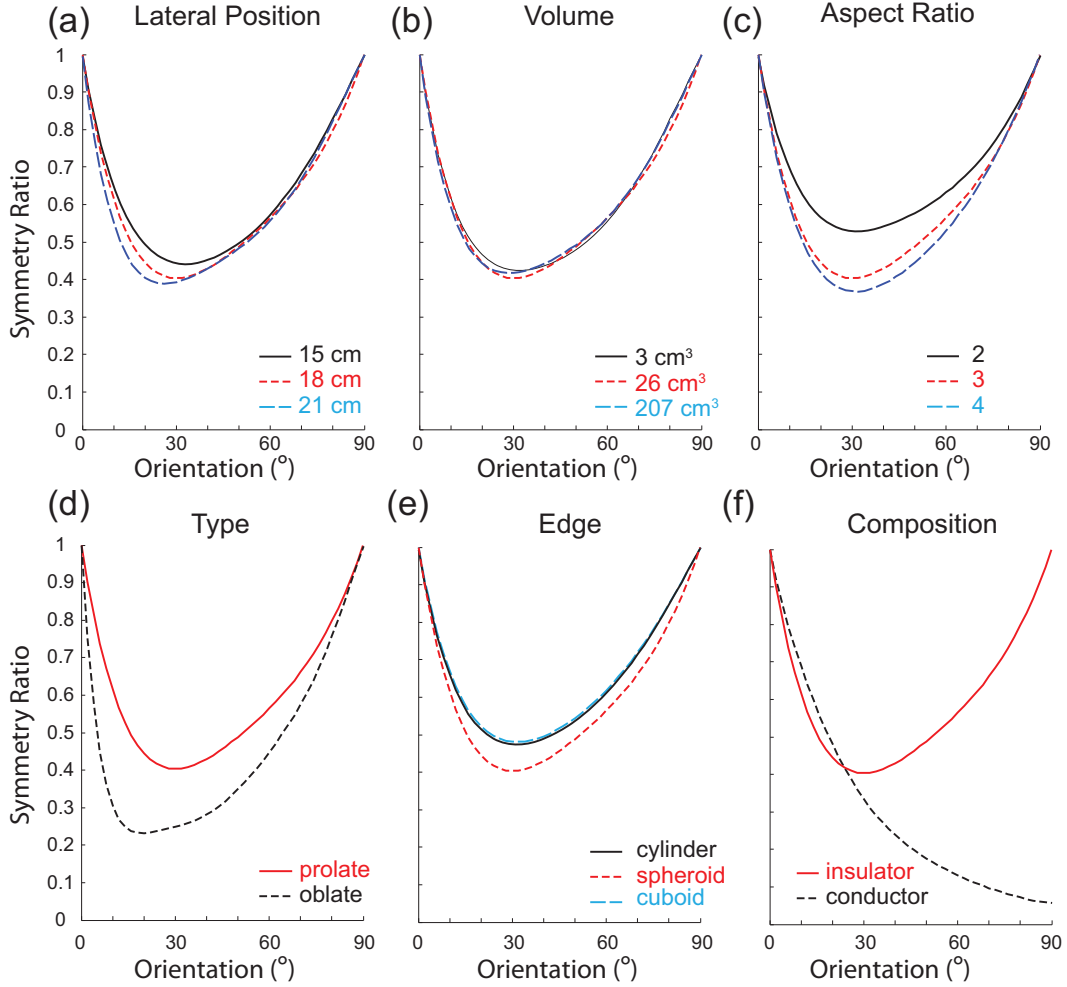
Fig. 6. Symmetry maps showing symmetry ratio as a function of orientation. (a) Prolate spheroids of volume 25.76 cm^3 and an aspect ratio of 3 at different distances. (b) Aspect ratio of 3 and distance of 18 cm with different volumes. (c) Distance of 18 cm and volume of 25.76 cm^3 with different aspect ratios. (d) Prolate and oblate spheroids of aspect ratio 3, volume 25.76 cm^3 and distance 18 cm. (e) Prolate spheroid, cylinder and cuboid of aspect ratio 3, semi-minor axis or short side 1.27 cm and distance 18 cm. (f) Conductive and insulating prolate spheroids of aspect ratio 3, volume 25.76 cm^3 and distance 18 cm.

map (Figure 5). After the robot rotates by $\beta°$ (Figure 3 (2)), a new translation is performed (Figure 3 (1)).

Active alignment works for prolate spheroids at any orientation angle (0° to 360°). Due to symmetry, only the orientation within the range 0° to 180° needs to be addressed. A spheroid of orientation Ψ at zero-crossing has an electric image that is the point reflection of a spheroid of orientation 180° − Ψ at zero-crossing. Thus, if a prolate spheroid at zero-crossing gives a symmetry ratio greater than 1 ($\eta_0 > 1$), this prolate spheroid has an orientation angle $\Psi_0 > 90°$. The SensorPod can treat it as a prolate spheroid with orientation $\Psi = 180° − \Psi_0$ by inverting the symmetry ratio ($\eta = 1/\eta_0$). The direction of rotation is also switched in order to rotate less than 90°. Therefore, only orientations from 0° to 90° need to be characterized.

For the specific case of a 90° orientation, the initial alignment is achieved when the orientation angle is at 90°. However, when identifying the aspect ratio, η_{AR} will be larger than 1. In this case, the SensorPod continues with

the active alignment as shown in Figure 3, (3) to (5), to ensure an orientation close to 0° at alignment.

For conductive prolate spheroids, the active alignment algorithm applies as before, but with the symmetry map for conductive objects. In addition, the calculation of the symmetry ratio is the inverse of the equation for non-conductive objects, as shown in Figure 3. The symmetry map for identically shaped objects differs for conductive and non-conductive prolate spheroids (Figure 6). All symmetry maps are generated with simulation data as presented in Section 4.

3.2. Estimation of aspect ratio

Following alignment, we rotate our robot to a specific orientation, 45°, and translate to the zero-crossing to estimate the prolate spheroid's aspect ratio. The choice of 45° is a trade-off and detailed in Section 7. The symmetry ratio η_{AR} is calculated at the new zero-crossing and used to
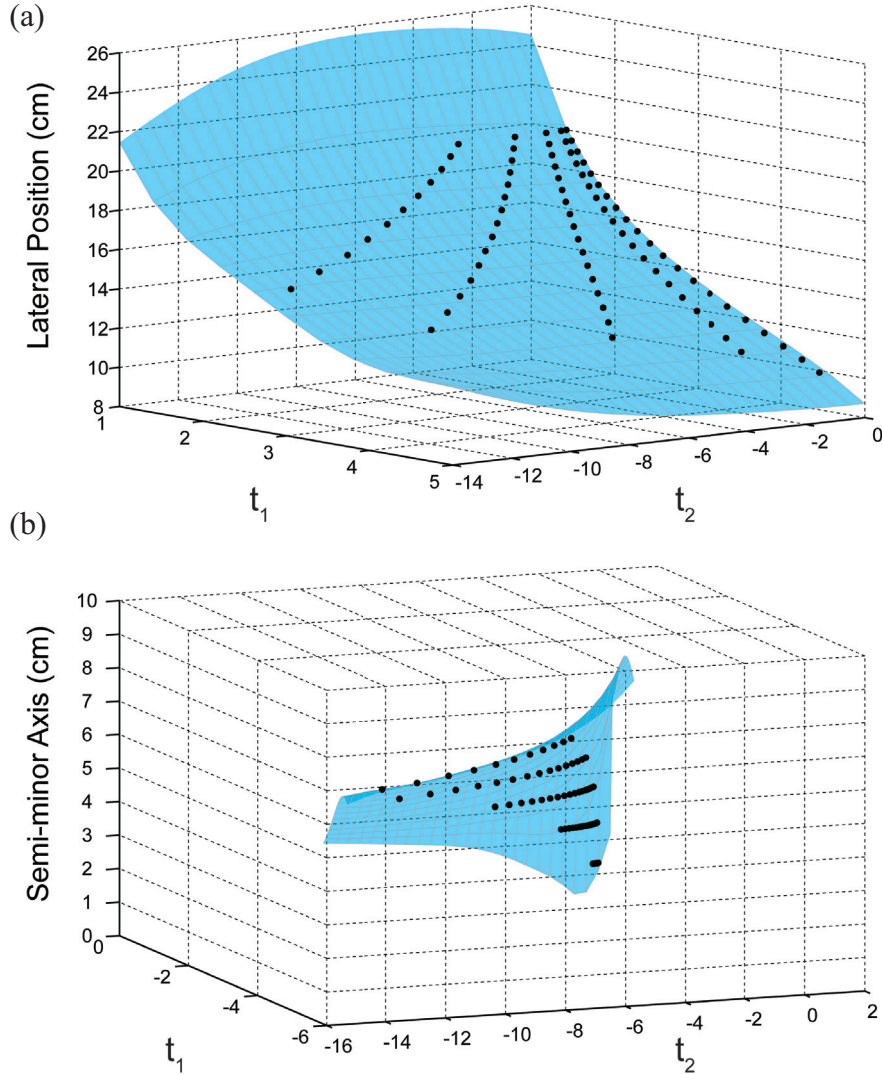
(a)

(b)

Fig. 7. GPR model for lateral position (*d*) estimation and semi-minor axis (*r*) estimation. The light blue surfaces represent the model's lateral position and semi-minor axis output given t_1 and t_2. (a) t_1 is V_{S4}/V_{S5} and t_2 is V_{S4}. (b) t_1 is V_{S4} and t_2 is V_{S5}.

estimate the aspect ratio from the relationship shown along the dashed vertical line of Figure 5 (also represented in Figure 3 (6)). Note that $\eta = 1$ for spheres.

For conductive prolate spheroids, a different curve derived from the symmetry map for conductive objects is used (blue curve in Figure 3 (6)).

3.3. Identification of spheres

With five pairs of sensors, we are able to identify the lateral position *d* and the semi-minor axis or radius *r* of spheres at the alignment position with no ambiguity. We use GPR (Rasmussen, 2006) to create a parameterless model for the estimation of *d* and *r* of insulating spheres. The model takes a 2D input converted from measurements and outputs the estimated *d* and *r* with their variances. The generation of

this model is detailed in Section 4. A visualization of the GPR model is shown in Figure 7. The black dots are the training dataset while the light blue surfaces are the mean of the estimated values given different t_1 and t_2. For clarity of presentation, the confidence region of the model is not shown.

3.4. Identification of prolate spheroids

With the uniform field assumption, we define two analytical models we consider for spheroid identification. A *uniform field exact analytical solution* refers to the relationship between the voltage perturbation caused by a spheroid in a uniform electric field and its pose and geometric properties. This solution is derived by solving Laplace's equation with boundary conditions (Bernhardt and Pauly, 1973; Landau

and Lifshitz, 1984; Clark, 2010). A *dipole approximation model* refers to the same relationship but derived by abstracting the spheroid as an electric dipole.

The GPR model allows us to identify the lateral position (distance) and radius of spheres when they are aligned with the SensorPod. For prolate spheroids, the aspect ratio complicates the identification process. In the uniform field exact analytical solution, the aspect ratio is embedded in the solution and is non-separable from other parameters. Therefore, it is useful to derive a simplified model where the aspect ratio is separable using approximation. In the following paragraphs, we derive the dipole approximation model which allows the separation of aspect ratio from other pose and geometric parameters. With this model, we are able to apply the sphere GPR model to estimate geometric properties of a spheroid.

A prolate spheroidal object in a uniform electric field can be approximated as an electric dipole (Landau and Lifshitz, 1984). This approximation improves as the object's distance increases, or as the spheroid's aspect ratio decreases. For our SensorPod, we consider the electrode on the side of the object to be the measurement point. The measurement of the other electrode in the sensor pair is considered to be unchanged. Applying the above approximation to our SensorPod, the measured differential signal at a sensor pair is written as

$$\Delta\varphi = \frac{\mathbf{R} \cdot \mathbf{P}}{|\mathbf{R}|^3} \tag{1}$$

where $\mathbf{R}$ is the position vector from the center of the object to the location of the measurement (Landau and Lifshitz, 1984), and $\mathbf{P}$ is the electric dipole moment of the object. *P*, if we use the axes of the spheroid as the coordinate system and if the electric field is parallel to the major axis of the spheroid, represents the scalar component of the dipole moment vector in the direction of the electric field computed as

$$P = \frac{1}{4\pi} E \cdot M \cdot V \tag{2}$$

where E is the uniform electric field strength, and V is the volume of the object. For prolate spheroids, V is given by

$$V = \frac{4\pi}{3} AR \cdot r^3 \tag{3}$$

where r is the semi-minor axis. M encodes the object's composition and aspect ratio. When the operating frequency is low, as in our case, M is given as (Landau and Lifshitz, 1984)

$$M = \frac{1 - \chi}{n_x + (1 - n_x)\chi} \tag{4}$$

Here, χ is the conductivity contrast factor equal to $\frac{\sigma_{water}}{\sigma_{object}}$, where σ_{water} and σ_{object} are the conductivities of the water and object respectively.

M can be simplified for insulators ($\sigma_{object} \gg \sigma_{water}$) and conductors ($\sigma_{water} \gg \sigma_{object}$) to

$$M = \begin{cases} \frac{1}{n_x - 1}, & \text{if insulator} \\ \frac{1}{n_x}, & \text{if conductor} \end{cases} \tag{5}$$

Here n_x is the depolarization coefficient (Landau and Lifshitz, 1984) along the major axis of the prolate spheroid. It is a positive value less than one but depends on the aspect ratio of the prolate spheroid. Further, n_x is analytically expressed as

$$n_x = \frac{1 - e^2}{2e^3} \left(\log \frac{1 + e}{1 - e} - 2e \right) \tag{6}$$

where e is eccentricity $e = \sqrt{1 - AR^{-2}}$. For oblate spheroids, see the supplementary material, Section 3. Specifically for spheres, n_x is 1/3. Thus, by equation (5), electric images of conductive spheres are twice the magnitude and opposite in sign from images of insulating spheres. Therefore the semi-minor axis and lateral position of conductive spheres can be identified with the GPR model for insulating spheres by scaling the electric image by 0.5 and inverting the sign.

The previous derivation allows us to estimate the lateral position and semi-minor axis of prolate spheroids from the GPR model for spheres. Using the dipole model, we scale the electric image of prolate spheroids first. Concretely, we examine the difference in the electric images of spheres and prolate spheroids. Combining equation (2), equation (3) and equation (5), we have equation (7):

$$P = \frac{1}{3} E \cdot M(AR) \cdot AR \cdot r^3 \tag{7}$$

If a prolate spheroid and a sphere have the same semi-minor axes (r) and lateral positions (d), the electric image of the prolate spheroid is related to that of the sphere by a factor of $\mathscr{F}$, as shown in equation (8). Therefore, with knowledge of the aspect ratio of the prolate spheroid, we are able to transform estimation of the lateral position and semi-minor axis length of a prolate spheroid into the estimation of the lateral position and radius of a sphere by scaling the prolate spheroid's electric image by $\mathscr{F}$ as

$$\mathscr{F}(AR) = \begin{cases} \frac{M_s \cdot V_s}{M_x \cdot V_x} = \frac{n_x - 1}{AR \cdot (n_s - 1)}, & \text{if insulator} \\ \frac{M_s \cdot V_s}{M_x \cdot V_x} \frac{1}{2} = \frac{n_x}{2 \cdot AR \cdot n_s}, & \text{if conductor} \end{cases} \tag{8}$$

Here subscript x indicates spheroids while s indicates sphere. n_x is the depolarization coefficient of a prolate spheroid; $n_s = 1/3$ is the depolarization coefficient of a sphere. The relationship between $\mathscr{F}$ and AR is shown by the curve in Figure 3 (7). The factor 1/2 for the conductor case is to scale the electric image of a conductive sphere to an insulating sphere.
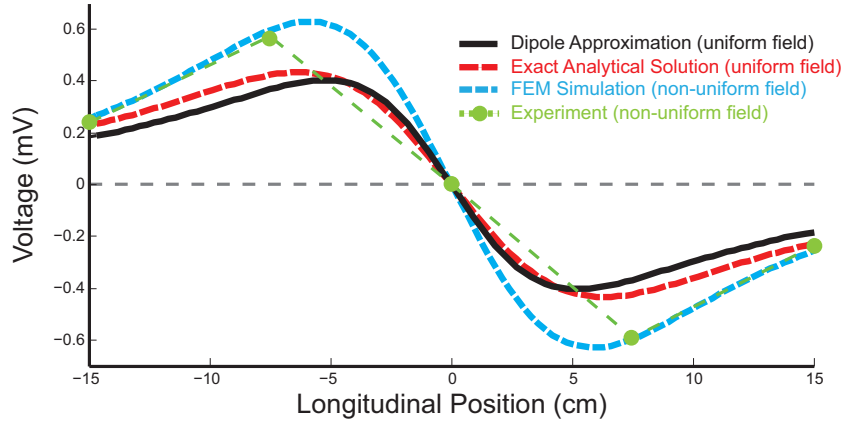
Fig. 8. Comparison of the electric images of the same object (aligned prolate spheroid, $AR = 3$, $r = 1.83$ cm, $d = 15$ cm, $p = 0$ cm) from three models. Based on the uniform field assumption, the dipole approximation model and exact analytical solution give similar results. The discrepancy between the electric images with these two approximations and those found through simulation and experiment is primarily due to the non-uniform electric field that is present in simulation and experiment. Error bars representing the standard deviation of 10 measurements for the experimental case are too small to be visible.

4. Model generation

We rely on FEM simulation to generate two key models, the symmetry map and the GPR model, used for active alignment and identification. We used the COMSOL (COMSOL Inc, Burlington, MA) multiphysics finite element software package as the numerical tool. The simulation is set up to match the experimental situation, and yields results very similar to experimental data (Figure 8). In addition, the simulated voltage perturbation at the sensors on the opposite side of the object is near zero. This validates our approximation that the distal sensor of each sensor pair has no voltage variation. The simulation is in 3D with a non-uniform electric field.

The basic geometric setup for the simulation involves a water body (2.1 m × 1.4 m × 0.6 m) with the SensorPod placed in the center. The tank walls and water–air interface are defined as insulating boundaries. The SensorPod is modeled with insulating material except for the excitation and sensing electrodes which are modeled as metal. The insulating shaft attached to the SensorPod was found to have negligible effect and therefore removed from the simulation. The effect of the tank walls will be covered in Section 7.

We use the AC-DC module of the COMSOL package for simulating materials with specified conductivity and permittivity values. We simulate the AC excitation signal using frequency domain simulation in the AC-DC module. Because the front and back excitation electrodes are 180° out of phase, one is given $+10$ V and one is given -10 V. The frequency domain simulation is set at 2 kHz to match the frequency of the excitation signal of the SensorPod.

The simulation of the differential mode signal between pairs of electrodes requires additional care due to its high sensitivity. In order to achieve higher accuracy, we simulate every scenario in two steps to remove the error caused by

meshing. First, the simulated spheroid is given the same material properties as water and the resultant differential signal is used as a baseline. Second, this baseline is subtracted from the differential signal from a second simulation where the spheroid is given the desired material property (metal for conductors, plastic for insulators). When simulating active alignment, the SensorPod remained stationary while the object was moved. This was done to avoid the large effect on the electric images that occurs when the simulated SensorPod's distance to nearby walls changes (the effect of the changing distance between the test objects and the tank walls was negligible). Table 1 summarizes the settings used for the simulations.

4.1. Generation of symmetry map

To generate the symmetry map, a non-conductive prolate spheroid of fixed volume (26 cm^3) was placed at a lateral position of $d = 18$ cm and simulated with orientations from 0° to 180° in increments of 3°. This was repeated for prolate spheroids of all aspect ratios presented in Figure 5. Symmetry maps for conductive prolate spheroids, insulating oblate spheroids, insulating cuboids and insulating cylinders were generated similarly and are presented in Figure 6.

4.2. Generation of GPR model

The GPR model for insulating spheres was generated with simulation results for non-conductive spheres at the alignment position. Sphere radii of 1.27 cm to 6.99 cm and lateral positions of 11 cm to 25 cm were used.

The electric image at alignment is symmetric with the middle sensor pair $V_{S3} = 0$ as shown in Figure 4(a). The electric image symmetry also implies that $V_{S5} = -V_{S1}$ and

Table 1. FEM simulation parameters. σ is conductivity and ϵ is relative permittivity, referring to vacuum's permittivity of 8.85×10^{-12} F·m^{-1}.

Model	Parameter	Value
Tank	Dimension (length, width, height)	2.1 m, 1.4 m, 0.6 m
	Water (σ, ϵ)	300 μ S/cm, 80
	Wall (σ, ϵ)	0 μ S/cm, 3
SensorPod	Shell dimension (length, radius)	45.72 cm 7.62 cm
	Shell (σ, ϵ)	0 μ S/cm, 3
	Excitation electrode radius	1.59 cm
	Sensing electrode radius	0.32 cm
	Electrode (σ, ϵ)	1,000,000 μ S/cm, 1
Mesh	Density	"Finer"
Excitation	Voltage	+ 10 V, − 10 V
	Frequency	2 kHz

$V_{S4} = -V_{S2}$. We therefore chose V_{S1} and V_{S2} as inputs to our models.

To train the GPR model for lateral position estimation, a transformation is applied to the electric image before it is used to generate the model.

We convert V_{S1} and V_{S2} from the symmetric electric image to a new vector (t_1, t_2) defined as

$$t_1 = \frac{V_{S2}}{V_{S1}} \tag{9a}$$

$$t_2 = V_{S2} \tag{9b}$$

The choice of division for t_1 is because the ratio of V_{S1} and V_{S2} is almost linear with the lateral position *d*, as shown in Figure 7(a).

To train the GPR model for radius estimation, the measurements V_{S1} and V_{S2} are used directly. We used the "Gaussian processes for machine learning" Matlab code package for the generation of the GPR model (Rasmussen, 2006). The details of training the GPR model are covered in the supplementary material, Section 4.

5. Implementation

5.1. Experiment

The experimental platform is shown in Figure 9 with the functional block diagram in Figure 10. There are two main components: a robotic positioning system (Figure 9(c)) which moves the SensorPod (Figure 9(a)). The positioning system is custom-built and mounted over a tank (2.1 m × 1.4 m × 0.8 m) filled with water to a depth of 0.6 m. The robot is able to move the SensorPod in *X*, *Y*, *Z*, and ϕ (yaw). The robot has high-precision encoders with a resolution of 100 μm in *X* and *Y*, 0.5 μm in *Z* and 0.06° in ϕ.
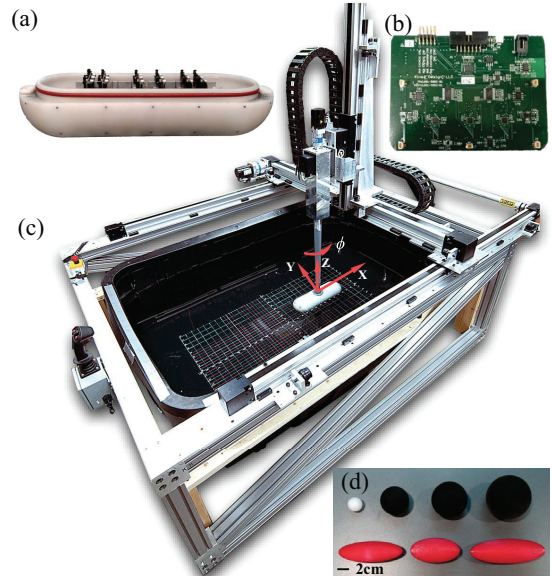

Fig. 9. Robotic positioning system, SensorPod, sensing electronics and test objects. (a) Bottom half of the SensorPod, showing position of custom sensing boards. (b) One of six sensing boards that process the signals from the 35 total sensing electrodes (only 10 used in this study). (c) The positioner is able to move the SensorPod (white cylindrical object attached via shaft) in *X*, *Y*, *Z* and ϕ. (d) Some of the test objects included 3D printed plastic objects (red), off-the-shelf rubber (black) and plastic spheres (white).

The SensorPod without the upper cover is shown in Figure 9(a) and is 45.72 cm in length and 7.62 cm in radius. The shell of the SensorPod is made of plastic and is attached to the robotic positioner with a metal shaft covered in insulating epoxy. The rod has negligible effect on the field at the mid-plane as has been verified in simulation (data not shown). All of the electrodes are made of stainless steel. The emitter electrodes are 1.59 cm in diameter, while the sensing electrodes are 0.32 cm in diameter. There are five differential pairs of sensing electrodes along the lateral aspect of the SensorPod (along the top edge of the bottom half, as shown in Figure 9(a)). The differential measurements are demodulated. The demodulation outputs are digitized by 24-bit Σ-Δ analog-to-digital converters.

Demodulation is applied to the differential voltage reading at the sensor pairs to extract the reading magnitude. Demodulation was achieved by multiplying a reference signal at the emitted frequency by the input signal (Shmaliy, 2006). This results in very high rejection of ambient electrical signals that are away from the frequency of the emitted field.

A block diagram is shown in Figure 11. We use square waves as both the excitation signal and reference signal. The circuit has an end-to-end differential gain of 101 with 50.5 from the instrumentation amplifier stage and 2 from
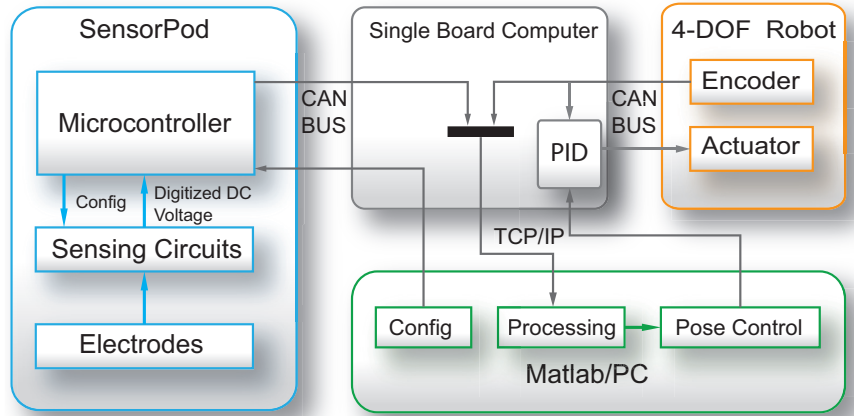
Fig. 10. Functional block diagram. A single board computer (black) running the QNX real-time operating system (QNX Software Systems Ltd, Ottawa, Canada) combines sensing data from the SensorPod (blue) and position data from the four-degrees-of-freedom (4-DOF) robotic positioner (orange) and sends it to Matlab/PC (green) for processing. The Matlab/PC interfaces the single board computer with TCP/IP and controls the position and orientation of the SensorPod via proportional-integral-derivative (PID) control, as well various settings, such as whether measurements are single-ended or differential.

the demodulation stage. Both the high pass filter (3 Hz) and low pass filter (LPF) (86 Hz) have unity gain (Figure 11). The circuit is grounded to earth ground through the robotic positioning system.

The water conductivity was 300 µS/cm. Non-conductive objects were used as test objects, with the exception of a 3D-printed insulating prolate spheroid wrapped in conductive aluminum foil (Table 2) which was used to show that the algorithm functions equally well for conductive objects. Spherical objects were off-the-shelf and made of rubber (6490K23, McMaster-Carr, Elmhurst, IL), while the prolate spheroids were custom 3D-printed in plastic. Object dimensions are given in Table 2. These test objects were attached to a metal rod (diameter 0.3 cm) that was insulated by heat-

Fig. 11. Differential sensing electronics. The voltage difference between the electrode pair is amplified by an instrumentation amplifier (IN-AMP) with a gain of 50.5. A unity gain high pass filter (HPF) removes the DC component of the amplified differential signal. The resultant signal is then demodulated by a reference signal of the same frequency. The output DC voltage is twice the amplitude of the amplified differential AC signal. The signal from the output of the demodulation stage (with high-frequency noise in blue) is further filtered by a unity gain LPF before being digitized by an analog-to-digital converter (ADC).

shrink tubing. The insulated metal holding rod was connected to a weighted base for stable positioning within the tank.

We performed active alignment followed by aspect ratio, lateral position and semi-minor axis estimation for our test objects. In practice, without the presence of an object, the SensorPod registers non-zero differential voltage readings that depend on the location of the sensor pair and the pose of the SensorPod. This effect is primarily caused by the relatively short distance (compared to the distance between the SensorPod emitters) to the non-conductive tank walls and tank water surface. Experimental active alignment requires measurement of this effect, which we term the "tank effect", as a calibration step prior to all subsequent measurements. The measurement occurs continuously over a 1.5 m × 0.8 m grid at the fixed SensorPod depth that was used for all experiments, which was 30 cm from tank bottom and 30 cm from the water surface. This mapping is repeated for yaw angles of 0° to 90° in steps of 5°. The measurement process establishes the relationship between the quintuple voltage offset vector (from five sensor pairs) and the pose of the SensorPod (X, Y and ϕ, with Z fixed). When the object is present, the SensorPod refers to an interpolated version of the map for every pose and position to subtract the tank effect, resulting in an estimate of the electric image of the test object. We placed the spheroids to be no less than several major axis lengths away from the tank walls so that the subtraction method is more accurate.
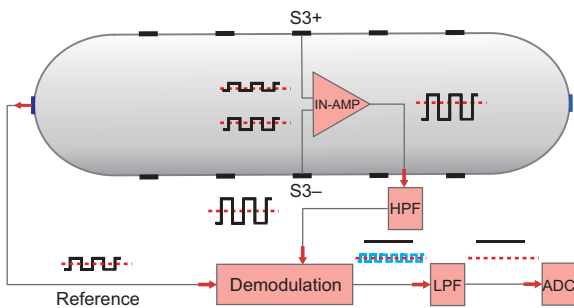
6. Results

6.1. Active alignment

Prolate spheroids starting at different orientations were simulated with two orientation estimation methods using the same platform as mentioned in Section 4. The

Table 2. Test objects.

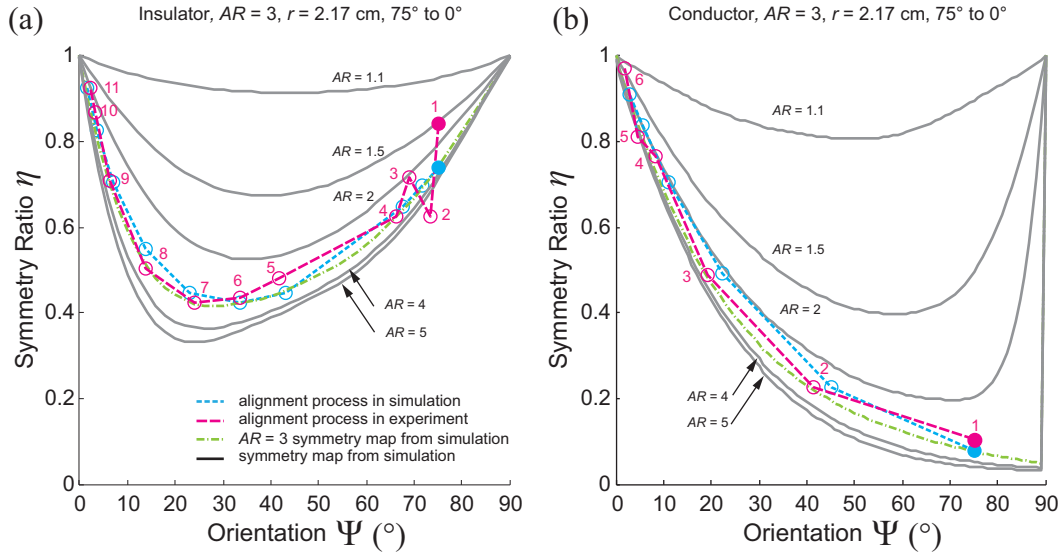| Item	Obj. 1	Obj. 2	Obj. 3	Obj. 4	Obj. 5	Obj. 6	Obj. 7	Obj. 8
Shape	Sphere	Sphere	Sphere	Sphere	Prolate spheroid	Prolate spheroid	Prolate spheroid	Prolate spheroid
Aspect ratio	1	1	1	1	2	3	3	3
Semi-minor axis (cm)	1.27	2.54	3.81	3.18	2.17	1.83	2.17	2.17
Material	rubber	rubber	rubber	plastic	plastic	plastic	plastic	aluminum (foil wrap)

Fig. 12. Example FEM simulation and experimental results for the alignment process, overlaid on symmetry maps. The alignment process starts with solid dots. (a) The SensorPod starts with a 75° orientation (solid blue and magenta dots) and decreases the orientation angle to 0° in the order shown. The amount of rotation is based on the smaller orientation angle of the two values estimated from the symmetry ratio. (b) The same configuration was repeated for conductive prolate spheroids.

simulated results are compared against experiments, and two selected examples for non-conductive and conductive ones are shown in Figure 12. In the figure, the symmetry maps are in gray and the curves corresponding to the aspect ratio of the object are marked green. The experimental results shown in both panels are examples of a typical alignment process.

We performed active alignment with five objects, each with 10 trials, with a success rate of over 90%. With a 0.90 threshold for the symmetry ratio η, the average terminal orientation error is 3°. The average longitudinal position error is less than 1 cm. Using the algorithm presented in Figure 3, the number of steps taken to converge varies with the initial orientation and the object's conductivity. In general, the smaller the starting orientation, the fewer steps needed for alignment. Conductive objects typically require fewer steps.

In the example shown in Figure 12(a), a prolate spheroid starts with an orientation of 75° and the SensorPod actively reduces the orientation angle by using the smaller value of the two angles estimated with the symmetry ratio, as previously discussed in Section 3.1. Figure 12(b) shows the same process of a conductor with the same geometry.

6.2. Estimation of aspect ratio

Several experiments were performed to assess the quality of the algorithm's estimate of aspect ratio, shown in Table 3 (standard deviation across 10 trials for each diameter/radius/aspect ratio combination shown). Note that d in the table denotes center-to-center distance as shown in Figure 2. To demonstrate the robustness of the aspect ratio estimate with distance, the prolate spheroids were estimated at different lateral positions from the SensorPod. Estimate error fell well within 10% with two exceptions. For the insulator spheroid with $AR = 3$, $r = 1.83$ cm and $d = 20$ cm, the error is 13%, and for the conductive spheroid with $AR = 3$, $r = 2.17$ cm and $d = 15$ cm, the error is 59%. We describe some reasons for these large errors in Section 7.

6.3. Identification of spheres and prolate spheroids

The identification of lateral distance and semi-minor axis was done after active alignment. For each trial with a certain parameter combination, we assume the object was already aligned with the SensorPod with uncertainty in longitudinal

Table 3. Aspect ratio estimation.

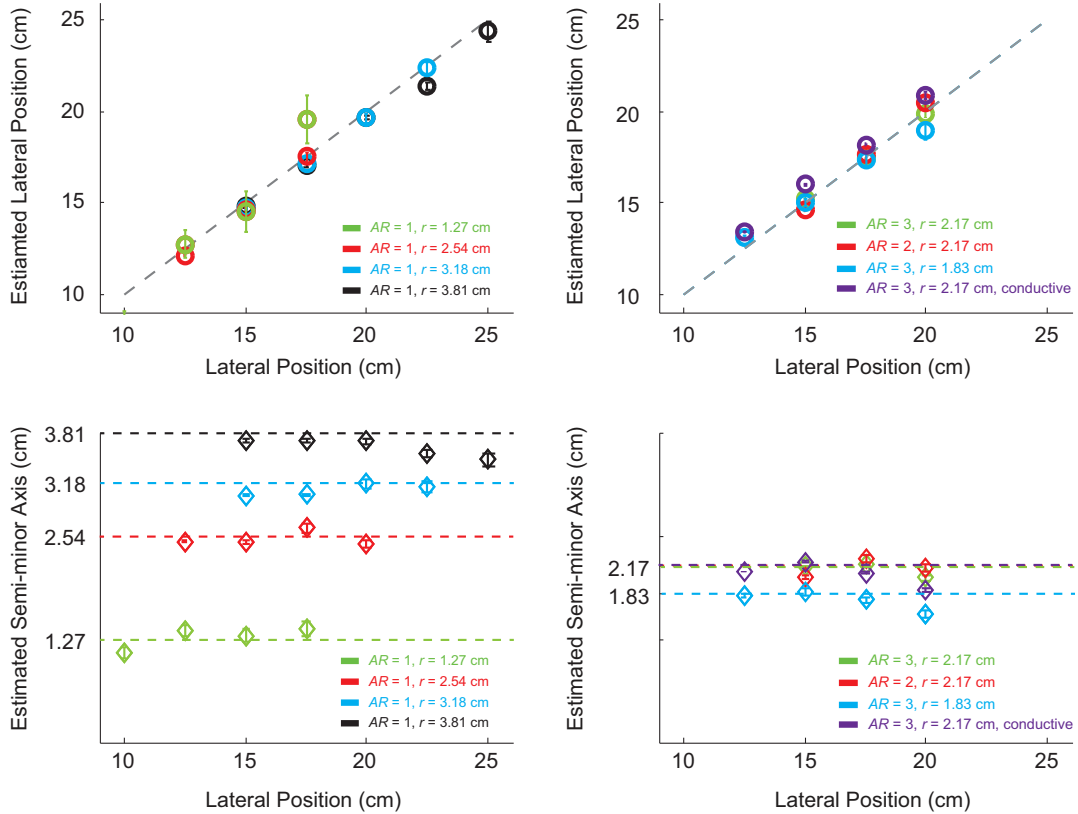| Item	AR =3, r =1.83 cm, insulator	AR =3, r =2.17 cm, insulator	AR =2, r =2.17 cm, insulator	AR =3, r =2.17 cm, conductor
d =15 cm	3.02 ± 0.22	2.99 ± 0.13	1.85 ± 0.07	4.78 ± 0.12
d =17.5 cm	2.89 ± 0.30	2.97 ± 0.29	1.97 ± 0.15	3.22 ± 0.14
d =20 cm	3.38 ± 1.15	3.03 ± 0.44	1.93 ± 0.13	2.96 ± 0.06

Fig. 13. Experimental estimation of prolate spheroid lateral position and size. Circle symbols represent distance estimation, while diamond symbols indicate semi-minor axis estimation. Green, red and blue symbols represent spheres of radii 1.27, 2.54 and 3.81 cm respectively. Each marker with error bars represents 10 separate trials for a certain configuration in aspect ratio, semi-minor axis, lateral position and electrical property. A separate trial is the average of 24 sensor measurements collected over a period of 20 ms for a certain configuration.

position and orientation comparable to that from active alignment.

Experimental results for sphere and prolate spheroid identification are shown in the left and right columns of Figure 13 respectively. For all four panels, the *x*-axis is the lateral position the object. In the estimation of lateral position (upper row of Figure 13), a dashed line is plotted to indicate agreement between estimation and actual values. For the estimation of *r*, at each semi-minor axis length (lower row of Figure 13) the same object was placed at different lateral positions.

Lateral distance and semi-minor axis estimation error is under 10%. In general, these errors increase as size decreases and lateral distance increases due to the corresponding diminishment of the strength of electric images.

7. Discussion

7.1. The relationship between an object and its electric image

Here we provide some intuition regarding the influence of several object properties on electric images (also see Multimedia Extension 1). Object size has a major impact on the corresponding electric image. The magnitude of the electrosense voltage reading scales almost linearly with the volume of the object.
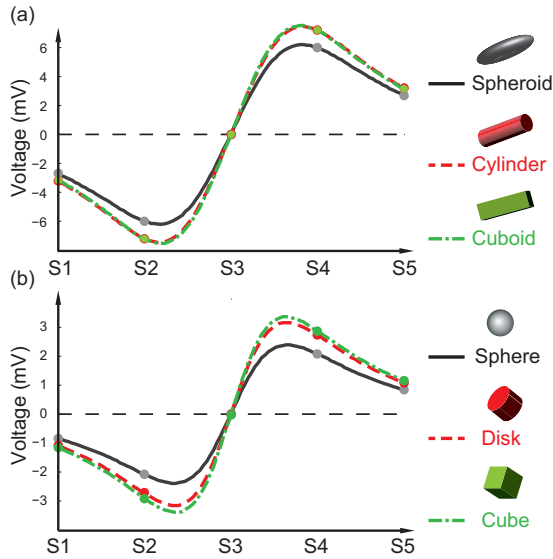
Fig. 14. Effect of object edges on their electric images based on simulation. All objects simulated are 100 cm^3 in volume and placed at the alignment position with the same lateral position (15 cm) from the SensorPod. (a) The electric images of a prolate spheroid, a cylinder and a cuboid; (b) the electric images of a sphere, a disk and a cube.
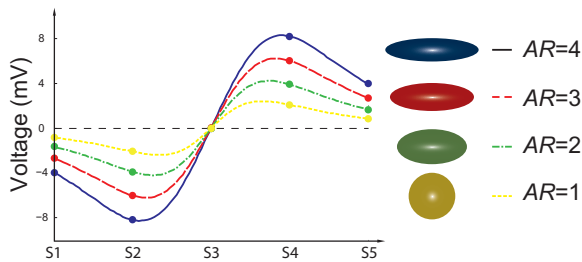

Fig. 15. Effect of aspect ratio on an object's electric image, from simulation. All simulated prolate spheroids are 100 cm^3 in volume and placed at the alignment position with the same lateral position (15 cm).

Longitudinal and lateral positions, although not inherent object properties, influence the electric images of objects significantly. The electric image magnitude drops approximately with the cube of lateral distance as indicated by our experiments as well as earlier work (Rasnow, 1996). Qualitatively, the longitudinal position influences the overall shape of the electric image, as shown in Figure 1(a) and (b). Compared to lateral position, the influence of longitudinal position is more complicated. This provides additional motivation for the active alignment stage of our algorithm.

Because of the diffusive nature of electrosense (Nelson et al., 2002), object edges are not pronounced in electric images. Symmetric objects of the same aspect ratio and volume are simulated at the alignment position and their electric images are shown in Figure 14. The influence of

edges is less clear than aspect ratio, especially when the major axis of the prolate spheroid is parallel to the major axis of the SensorPod.

As seen in equation (2), aspect ratio has a major influence on the electric image. We simulated insulating objects of the same volume and lateral position but different aspect ratios at alignment position. The comparison of their electric images is given in Figure 15. The influence of aspect ratio is even more pronounced when the object is conductive as indicated by equation (5). This is because a conductive object is shorting part of the relatively high resistance signal pathway (water). The change in effective resistance caused by a conductive object in this medium is higher than the corresponding change caused by a non-conductive object.

Object conductivity influences the electric images as reflected in equation (5). However, the absolute conductivity is less important than the difference in conductivity between the object and the fluid (Rasnow, 1996; Bai et al., 2012). Therefore by "insulator" and "conductor" we mean objects whose conductivity is much lower or much higher than that of the surrounding water, respectively. Water has a wide range of conductivities, from 1–100 µS/cm common in the habitats of electric fish (MacIver et al., 2001) to an upper bound of 56,000 µS/cm for seawater (Culkin and Smith, 1980). As suggested by our previous work (Solberg et al., 2008) and by Servagent et al. (2013), although all experiments discussed here were in freshwater, the SensorPod is able to work in saltwater environments as well. However, to maintain performance at freshwater levels, in saltwater our SensorPod needs to increase the power of the emitters (currently 0.5 W) by a factor of approximately 100.

If the conductivity contrast factor $\chi = \frac{\sigma_{water}}{\sigma_{object}}$ approaches unity, factor M will approach zero (equation (4)). Thus, the amplitude of the electric image, $\Delta\phi$ (equation (1) and equation (2)), approaches zero, resulting in reduced performance in detection and identification of the target. Note that this is not a limitation of our algorithm because the object is very similar to water. For example, if a hypothetical blob of liquid has half of the conductivity of water, the identification algorithm will estimate the object to be an insulator with a size that is smaller than the actual size. As a rule of thumb, if the conductivity of the water and object differ by one order of magnitude or more, our size estimation algorithm will deliver reasonable estimates. In reality, for most real-world inanimate objects, the conductivity is either orders of magnitude smaller than that of water (such as rubber) or orders of magnitude larger than that of water (such as metal). Live animals and plants do not necessarily fall into either category (Nelson et al., 2002), and would likely need capacitive sensing for their correct estimation. For capacitive objects, even if their contrast factor is unity, the object can be detected with capacitive sensing, as shown in our previous work (Nelson et al., 2002; Bai et al., 2012).

7.2. The dependence on motion and comparison to approaches without motion

Having discussed the complex relationship between object geometric properties and their electric images, here we motivate the crucial reliance on motion in our algorithm.

7.2.1 Motion versus supervised learning. In this study, the use of motion allows the estimation of longitudinal position and orientation separately. It reduces the complexity of the estimation task of five geometric properties and allows the use of one GPR model trained by simulation data from spheres.

To appreciate the importance of motion for the algorithm we have presented, consider an alternative that relies solely on supervised learning to estimate all properties without movement. Here we revisit the simple case of sphere identification (radius r, longitudinal position p and lateral position d) in a uniform electric field. The electric image of the sphere is calculated analytically using equation (1). Even in the absence of noise, the building of a supervised learning model to estimate all three properties has failed with several regression and dimensionality reduction methods (data not shown). The attempted regression methods included linear regression, GPR, and symbolic regression (Schmidt and Lipson, 2009), while the attempted dimensionality reduction methods include Kernel PCA, Isomap, LLE, among others (Matlab drtool toolbox). The main issue is that the learned model gives rise to very large levels of uncertainty for certain measurement inputs. While the above is not a proof, it is clear that the use of supervised learning methods to identify a sphere in a uniform electric field is already a difficult problem. We can obtain insight into the source of the difficulty from the following perspectives.

From the perspective of electrosense physics, the effect of both radius r and lateral position d is intensification or attenuation, which does not alter the overall shape of the electric image. Meanwhile, the aspect of the electric image that is affected by changes in r and d, the amplitude, can be challenging to disentangle, since an increase in r has effects similar to a decrease in d. Longitudinal position p affects the shape of the electric image as shown in Figure 1(a) and (b). For a sphere in a uniform field, p is the same as the zero-crossing position of the electric image on the SensorPod. Note that this is a continuous feature of the electric image which is not available when the number of sensors is limited. But this continuous feature is readily available when motion is used: the SensorPod can simply track the voltage reading of the middle sensor pair to estimate p.

From a mathematical perspective, while computing the electric image of an object is fairly straightforward using analytical methods for isolated simple objects or simulation for more complex cases, the inverse problem is closely related to the Calderón problem (Calderón, 2006), which is typically severely ill-posed (Dines and Lytle, 1981). Without moving, the sensing device has to vary the electric field configuration in order to estimate geometric properties (Snyder et al., 2012).

Through movement, our algorithm removes p and Ψ from the unknowns through the active alignment process. It also enables the separation of AR from the remaining two parameters, d and r, so that a relatively simple supervised learning model can be built to deal with only two parameters. In addition, supervised learning without the aid of motion faces the "curse of dimensionality" where the training dataset size exponentially grows with the number of unknown properties (Friedman, 1997; Jimenez and Landgrebe, 1998). In our case, when building the model, we use 11 variations for each parameter. As a result, the dataset for only five parameters is on the order of 11^5 or 100,000, compared to 100 for two parameters.

From a biological perspective, as for all active sensing organisms, motion is a very salient aspect of sensory acquisition in electric fish (MacIver et al., 2001; Nelson and MacIver, 2006). The fish actively uses both motion and tail bending when identifying underwater objects (Assad et al., 1999; Stamper et al., 2012; Hofmann et al., 2013). Both motion and tail bending give the fish different perspectives and additional information to identify objects. Similar approaches have been studied in simulation for object identification by Ammari et al. (2013, 2014) and Snyder et al. (2012). Other common examples of movement for sensory acquisition include eye movements and movement of the sonar probe in echolocating bats (Land, 1999; Yovel et al., 2010; Patterson et al., 2013). For example, when identifying object geometry using vision, animals move closer and foveate. Based on the previous analysis, even though a fully supervised learning might be possible, it is computationally inexpensive and convenient to use motion to identify object geometric properties. It seems likely that the computational simplicity of electric image analysis afforded by movement partially explains why motion is integral to sensory acquisition in electric fish.

Having motivated the use of motion in reducing algorithm complexity, we now discuss the alignment position and sensor placement in the context of a convenient measure of the information content of electric images, Fisher information (Frieden, 2004; Silverman et al., 2013; Miller et al., 2014; Neveln et al., 2014). Again, we use the idealized case of a sphere in a uniform field. As shown in the supplementary material, Section 5, for a single sensor pair, the longitudinal position of the SensorPod that yields the most information with respect to the longitudinal position of an object is the alignment position. The longitudinal position of the SensorPod that yields the most information with respect to radius r and distance d is away from the center. Consistent with the Fisher information, we use the middle sensor pair to determine when the SensorPod is in the alignment position ($p = 0$), and the off-center sensor pairs for distance and size estimation; see equation (9). The Fisher information motivates the use of motion for the SensorPod to get to locations where the information density is higher. It also shows that it is advantageous to have

multiple sensors at the alignment position in order to maximize the Fisher information with respect to the object parameters of interest.

The above mathematical analysis also helps to inform the number and placement of sensors in robotic electrosense. Two closely placed sensors tend to yield similar measurements. Thus, an increase in the number of sensors on the mid-plane of the SensorPod results in a marginal increase in the amount of information gathered. It is instructive to consider the minimal sensor configuration to perform the estimation. For the disambiguation of r and d alone at the alignment position, two differential sensor pairs are sufficient (only S4 and S5 were used in the generation of the GPR above). For active alignment, an additional three differential sensor pairs are needed, two at positions away from the center, symmetric to the first two pairs (S1 for S5, S2 for S4; see Figure 5), and one pair at the center (S3).

7.2.2 Comparison with approaches without motion. The localization and identification of underwater objects with electrosense is a difficult task. We compare our approach to prior work in object localization and identification.

Both the EIT approach (Snyder et al., 2012) and the multi-frequency (or multi-position if one frequency is allowed) approach (Ammari et al., 2013, 2014) share the similarity of constructing a measurement matrix. In Snyder et al. (2012), every row of the measurement matrix corresponds to a unique excitation-sensing configuration, while in Ammari et al. (2013, 2014) data in every row is collected at a unique frequency (or unique position if only one frequency is allowed). The use of a measurement matrix requires expensive computation using a forward model and search in order to reconstruct the impedance and location probability map, respectively. A measurement matrix is constructed to obtain different "perspectives": different field configurations in the case of Snyder et al. (2012), different frequency measurements in the case of Ammari et al. (2013), and different locations in the case of Ammari et al. (2014).

Our approach gains different perspectives with sensors at different locations and active motion. With the active motion strategy, we reduce the amount of computation required. We approach the overall difficult task by solving smaller problems sequentially, in contrast to reliance on computation to estimate all properties at once.

7.2.3 Motion dynamics. During active alignment, the motion of the SensorPod is controlled by the robotic positioner with direct pose commands. For both translation and rotation, the SensorPod is moved at a velocity that does not cause major water disturbance. This is to ensure a stable and reliable boundary condition, since the air–water interface acts as an insulator that confines the electric field in the same way as the non-conducting walls.

The motions used in this work are rather simple and straightforward: separate translation and rotations. Optimal

motion control methods exist to increase the active alignment speed through smoothly combining these movements.

7.3. Characteristics and assumptions of each stage of the algorithm

7.3.1 Initial conditions. In Section 1, we assume the object of interest starts within the detection range of the SensorPod. To bring the object within range, active electrosense search algorithms need to be applied (Solberg et al., 2008; Silverman et al., 2013; Miller et al., 2014; Neveln et al., 2014). These approaches work for spheres, which is a good approximation for spheroids at a distance. The object should not be on a course of collision for the initial SensorPod translation and the rotation after alignment. Reactive control algorithms (Dimble et al., 2014) or simple thresholding techniques can be employed to avoid collision.

The direction of initial translational motion is bidirectional. If the SensorPod moves out of detection range without sensing a zero-crossing, the SensorPod moves in the other direction. Subsequent translational motions are unidirectional and converge to the alignment position as covered in the supplementary material, Section 2.

There is a simple procedure to disambiguate insulating and conductive spheroids at the first stage of the algorithm. This procedure involves single-ended measurement of the electric field perturbation (with respect to the circuit ground of the SensorPod electronics) in contrast to the differential measurements discussed thus far. Single-ended measurement refers to the demodulation of the AC voltage reading from a single electrode (with respect to circuit ground) on either side of the SensorPod. This method of measurement gives direct information about the voltage perturbation on one side of the SensorPod, allowing us to know which side of the SensorPod the object is on. Knowing this, we are able to disambiguate insulating and conductive objects from the sign of the electric image at different sensor pairs (for example, compare Figure 1(a) and (c)). In our case, whether the SensorPod is in single-ended versus differential measurement mode is software-controllable.

7.3.2 Active alignment. Comparing the blue (simulation) and red (experimental) symmetry ratio versus orientation angle curves for the sample active alignment shown in Figure 12, while the overall trend is good agreement, the agreement is not perfect. There are at least four causes of gaps between experimental and simulated active alignment. First, voltage offsets at sensor pairs vary over time even when the pose of the SensorPod (X, Y, Z and Φ) remains the same. This variation is likely due to the electrochemistry at the electrode–water interface and will be further discussed in Section 7.3.5. Therefore, our map of the voltage offsets (obtained during the tank effect measurement step mentioned above) becomes less reliable over time. Second, the voltage offset associated with a random pose relies on the interpolation of the tank effect map, resulting in

inaccuracy for certain poses. Third, the symmetry map in Figure 5 is from simulation and differs slightly from the values measured experimentally. Fourth, during the experiments, the zero-crossing is detected by using a threshold on the voltage reading, so the symmetry ratio that is calculated is also slightly different from the one that would be obtained if the robot was located at the true zero-crossing position.

Despite these sources of error, the alignment phase of the algorithm is robust. Every iteration is independent of prior iterations, provided that the object is still within the SensorPod's detection range and not on a collision course. Thus, if a prior iteration experiences excessive noise or garbled data, the next iteration is able to correct for this. In more than 50 trials with different objects, the alignment position was achieved with a success rate of better than 90%.

The accuracy of orientation alignment depends on the threshold of the symmetry ratio and the aspect ratio of the prolate spheroid as shown in Figure 5. For a symmetry ratio threshold of 0.90, the accuracy of orientation is less than $3\,^\circ$ for an $AR = 3$ prolate spheroid and less than $6\,^\circ$ for an $AR = 1.5$ prolate spheroid.

The accuracy of longitudinal position alignment is typically better than 1 cm. Longitudinal position alignment accuracy is derived from orientation alignment accuracy by referring to a longitudinal position offset map. A longitudinal position offset map is similar to the symmetry map where the longitudinal position at zero-crossing is plotted against orientation angle, as shown in the supplementary material, Section 2. Such maps reveal, at zero-crossing, a small orientation angle corresponds to a small longitudinal position offset. Therefore, we extrapolate the longitudinal alignment errors given the orientation alignment errors. Prolate spheroids with AR less than 1.2 are always considered aligned regardless of the orientation angle.

The symmetry map is an important component in active alignment. We rely on simulation to characterize the sensitivity of the symmetry map to certain geometric properties. In Figure 6(a), (b) and (c), insulating objects with varying lateral position, volume and aspect ratios are simulated. The symmetry map is almost invariant of size and lateral position but is sensitive to the aspect ratio.

7.3.3 Estimation of aspect ratio. We estimate aspect ratio based on the symmetry map generated from simulation. According to the symmetry map (Figure 5), estimation becomes more difficult when orientation angles approach $0\,^\circ$ or $90\,^\circ$ where the curves associated with different aspect ratios converge. For the same reason, it would appear optimal to estimate aspect ratio at around $20\,^\circ$ where the individual curves are more "spread out". However, Figure 6 also shows that the symmetry map associated with one aspect ratio also varies slightly with the size and lateral position of the object and that this variation is less pronounced at higher orientation angles. In this sense, we want to choose a region where such undesirable variation is

minimal. Balancing the two factors, we choose to estimate aspect ratio at $45\,^\circ$.

Here we compare the method we employed with an alternative as suggested by the uniform field dipole approximation model that separates aspect ratio from other geometric properties (equation (2)). For the same prolate spheroid, if two electric images are taken at $0\,^\circ$ and $90\,^\circ$ while $p = 0$, the voltage ratio of their electric images at V_{S4} is related to the aspect ratio with a one-to-one mapping. For the $90\,^\circ$ case, M is related to n_y, the depolarization coefficient along the minor axis, instead of n_x. Under the uniform field assumption, the above one-to-one mapping is invariant to lateral position and size. This desirable property no longer holds in the experimental situation where the field is non-uniform. The estimated aspect ratio deviates from the actual value, and the deviation depends heavily on the size and lateral position of the object, rendering this approach less useful. In the symmetry-map-based estimation method, the non-uniform field effect is already reflected in the construction of the symmetry map. This explains why the symmetry map approach works better than estimates based on a uniform field approximation.

For aspect ratios larger than 5, the symmetry map tends to converge, making the estimation of aspect ratios larger than 5 more difficult. This is because as the aspect ratio increases, the object asymptotically resembles a wall whose length variation contributes little to the variation observed in electric images. We can also observe this effect in our function $\mathscr{F}$ relating aspect ratio to the factor needed to scale the electric image to the nearest equivalent sphere (Figure 3 (7)). The function appears to flatten beyond aspect ratios of 5, which implies that the electric images of prolate spheroids with large aspect ratios are indeed similar. Similar to the estimation of orientation, the estimation of aspect ratio is ineffective for prolate spheroids with AR less than 1.2.

We noted two cases where there were large errors in aspect ratio estimation: for the smallest insulator at the largest distance (estimated $AR = 3.4$, actual $AR = 3$), and for the largest conductive spheroid at the shortest distance (estimated $AR = 4.8$, actual $AR = 3$) (Table 3). The accuracy of all estimates from the algorithm diminishes as electric image intensity declines, which resulted in the error for the small distant insulator. For the close conductive spheroid, the large error is due to a decline in accuracy of the uniform field dipole approximation model for the intense electric images of conductive objects as the distance between the object and SensorPod becomes very small (in this case $d = 15$ cm, meaning the edge-to-edge distance was $15 - 7.62 - 2.17 = 5.21$ cm).

7.3.4 Identification of spheres and spheroids. The estimation of the lateral position d for both spheres and prolate spheroids is accurate with small variance, as shown in Figure 13. The performance depends heavily on the signal-to-noise ratio (SNR). Since the noise level is stable, the
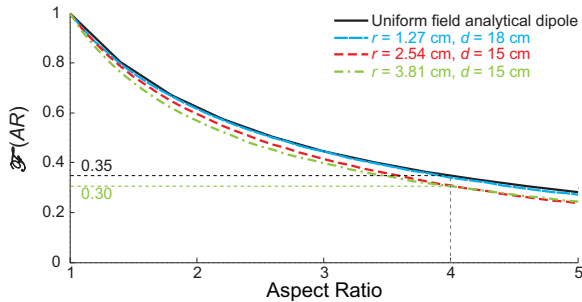
Fig. 16. Comparison of $\mathscr{F}(AR)$ and simulation results. Simulated objects with semi-minor axes of 1.27 cm (blue), 2.54 cm (red) and 3.81 cm (green) are placed at longitudinal distances of 18 cm, 15 cm and 15 cm respectively. For one category of objects represented by the green curve, the estimation of $\mathscr{F}$ when $AR = 4$ is about 16% higher. This percentage error increases as AR increases.

performance depends on the strength of the electric image. For example, for the sphere with a radius of 1.27 cm, the estimation starts to deviate from the true value as the lateral distance increases.

The estimation of semi-minor axis r also deteriorates as the SNR decreases. The estimation for spheres is more accurate than for prolate spheroids because the scaling (equation (8)) introduces error. Nonetheless, it is still reliable to estimate the semi-minor axis regardless of the aspect ratio and volume, as shown in the estimation for prolate spheroids with a semi-minor axis of 2.17 cm and different aspect ratios.

In Figure 8 we compare the electric images from the uniform field dipole approximation, the uniform field exact analytical solution (Section 3.4), FEM simulation, and experiments for the same scenario of a non-conductive prolate spheroid at the alignment position. For the same configuration, simulation produces results very close to experimental values ($< 5\%$ difference). This also validates use of a GPR model trained with simulation data in the experimental work. There is a clear discrepancy in the electric images generated from the two analytical models and simulation. The main reason is the difference in the electric field: simulations and experiments involve a non-uniform electric field while the two analytical solutions assume a uniform field.

Regardless of the discrepancy due to electric field structure, the method of scaling the electric image of prolate spheroids to a hypothetical sphere (based on the uniform field dipole approximation) for identification in non-uniform electric fields (Figure 3 (7)) performs well. In simulation, we computed the relationship between the scaling factor and the aspect ratio of objects with different sizes and lateral positions and compared the results with $\mathscr{F}(AR)$, as shown in Figure 16. Overall, the accuracy of $\mathscr{F}(AR)$ as an approximation from experiment depends on the aspect ratio, size, and lateral position of the object. The accuracy increases as the aspect ratio and size decrease and lateral

position increases. This is because when an object's aspect ratio approaches unity, when the object is reduced in size, or when it is further away, it is better approximated as a dipole. Even with the case of a large object with $r = 3.18$ cm, $AR = 5$ and placed at $d = 15$ cm, the error in the scaling factor is less than 10%.

7.3.5 Non-ideal effects in experiments. Noise in the system stems from four sources. The circuit has inherent noise from the components (Horowitz et al., 1989). To characterize these effects independently, we moved the SensorPod out of the water and passed electrical signals through a resistor network while measuring the voltage across a sampling resistor. The measured RMS noise is shown in Table 4.

The high power motors that move the SensorPod add high frequency noise when turned on, also shown in Table 4. The most unpredictable sources of noise are from the electrochemistry at the electrode–water interface (Legat and Doleček, 1995; Cottis, 2001; Tallgren et al., 2005) and inhomogeneous resistivity of water. Both sources of noise appear mostly as drift: low-frequency, long-term instability in voltage measurements. In our study, drift is in the demodulated DC voltage from the input AC voltage, which has the same frequency as the reference signal. In this sense, the drift is essentially the variation in the amplitude of the AC signals at the sensor pairs. DC drift at the sensor pairs is eliminated by the LPF after the demodulation stage because the frequency of the DC drift is different than that of the reference signal in the demodulator. The noise in Table 4 is measured as the differential voltage from the middle sensor pair for a period of 300 s. The values are calculated as RMS noise. For normal operation with the robotic positioning system motors on, the dynamic range is around 50 dB.

Noise limits the detection range of the SensorPod. For example, with a noise floor of 1 mV, a non-conductive sphere that is 1.27 cm in radius is undetectable beyond a lateral position of 20 cm. The goal of object identification sets a higher standard on the SNR because it requires distinguishable signals over multiple sensors. In practice, when the object is aligned, we consider SNR=20 dB to be the threshold where the object's r and d can be estimated. This SNR of 20 dB requires the noise floor to be under 100 μV for the non-conductive sphere with radius 1.27 cm at a lateral position of 20 cm.

Another major non-ideal effect is the presence of non-zero differential voltage readings at each sensor pair when no object is present. This non-zero reading varies from

Table 4. Sources of noise.

Scenario	AC noise (μ V)	Drift (μ V)
Dry-dock	3.1	10.2
Gantry off	6.1	18.6
Gantry on	58.6	25.5

sensor to sensor and depends on the pose of the SensorPod. The voltage offsets are extremely sensitive to the orientation angle of the SensorPod. One part of the voltage offset arises from the electronics, primarily due to the analog demodulator. Another and a more important part of the voltage offset is due to the proximity of the non-conducting tank walls and tank water surface. The effect of the tank wall and air–water interface is equivalent to multiple images of the SensorPod mirrored by the boundaries with the dielectric image method (Jackson and Jackson, 1962; Dimble et al., 2014).

As previously described, the tank effect necessitates a calibration step in which it is measured across all positions and orientations. At a fixed Z position with no object present, every pose of the SensorPod (X, Y and ϕ) corresponds to a five-dimension vector. The voltage offset is subtracted as a base value when measuring the electric image of an object.

Limited tank space also induces movement of the water surface when the SensorPod is moving. This changes the electric field structure by effectively changing the distance to the non-conducting boundary of the tank water surface, causing "noise" in measurements. When the SensorPod is moving at 3 cm/s in water, this effect causes instability of up to 200 μV in the readings. When creating the tank effect map, this noise can be filtered out. However, when the SensorPod is actively aligning with an object, this noise can affect the zero-crossing position, and therefore result in some error in orientation angle and longitudinal position estimation. Both the tank effect and water surface variability effect would be greatly diminished with depth, and would be unlikely to be a concern in most field conditions.

7.4. Extensions of the algorithm

The active alignment and identification approach was performed with prolate spheroids. For oblate spheroids, we assume the oblate spheroid's minor axis is within the plane of sensors and only yaw angle is considered. Figure 6(d) compares the simulated symmetry map of prolate and oblate spheroids of the same volume, lateral position and aspect ratio. The two curves are similar qualitatively, but the prolate curve shows greater variation in symmetry ratio. This is because the oblate spheroid perturbs the electric field more extensively in the Z direction due to its larger dimension along that axis, which is not being measured. The scaling factor $\mathscr{F}$ can be calculated with equation (8). The depolarization coefficient is calculated differently as shown in the supplementary material, Section 3. Symmetric objects like cuboids and cylinders also show qualitatively similar symmetry maps as shown by Figure 6(e). The scaling factor for these types of objects, however, could be approximated with that of prolate spheroids.

A more general scenario is the situation where the spheroid's major axis is not within the plane of the sensors and field emission electrodes. Hence two additional parameters, Z-direction offset z from the center of the SensorPod, and pitch angle γ, are to be identified. We first examine how our algorithm could be adapted to address two simplified

3D pose cases: (1) $\gamma = 0$, $z \neq 0$ and (2) $z = 0$, $\gamma \neq 0$. For the first scenario, an additional motion in the Z-direction after the first zero-crossing brings the prolate spheroid in plane with the sensors. This Z-direction motion stops when the maximum electric image strength is obtained. For the second scenario, an additional rotation in the pitch direction after the first zero-crossing brings the major axis of the SensorPod parallel with that of the prolate spheroid. This rotation also stops when the maximum electric image strength is obtained. The case where both z and γ are non-zero is more challenging. Using active translation in the Z-direction and rotation in pitch, the two parameters may be reduced to zero with additional measurement data from circumferential sensors. Similar to the identification of yaw orientation angle and longitudinal position, the identification process may also need to be simultaneous.

Our algorithm can be applied to capacitive objects. However, the object could be classified as either an insulator or a conductor depending on its capacitance and the frequency of the electric field used. In addition, the estimated size will be less than the actual size due to a reduced electric image magnitude.

In future work, we will extend the algorithm to include a third stage to identify the composition of the object. Referring back to the dipole approximation model in equation (2), composition is only included in M. For homogeneous capacitive objects, the permittivity and conductivity information can be extracted with an analytical model and measurement at multiple frequencies.

8. Conclusion

Active alignment and identification of objects underwater is a complex task involving convoluted and non-linear relationships between multiple object properties and multidimensional electric images. In this study, we employed an active motion and supervised learning approach that first aligns with prolate spheroids and then identifies object size and shape in a sequential manner. The use of active motion reduces the complexity of the problem and allows for the use of a simple supervised learning model. In both simulation and experiment, we demonstrate estimation of object geometric properties with a reasonable level of accuracy. We also discuss how this approach can be extended to other types of objects, as well as objects that are at an arbitrary orientation with respect to the artificial electrolocation system. Our study provides insights into the nature of electric images, the implementation of robotic electrosense, and the ubiquity of motion in the sensory acquisition strategies of the biological model system that inspired the present work, the weakly electric fish.

Funding

References

Alamir M, Omar O, Servagent N, et al. (2010) On solving inverse problems for electric fish like robots. In: *IEEE international conference on robotics and biomimetics (ROBIO 2010)*, Tianjin, China.

Ammari H, Boulier T and Garnier J (2013) Modeling active electrolocation in weakly electric fish. *SIAM Journal on Imaging Sciences* 6(1): 285–321.

Ammari H, Boulier T, Garnier J, et al. (2014) Shape recognition and classification in electro-sensing. *Proceedings of the National Academy of Sciences* 111(32): 11,652–11,657.

Araujo EG and Grupen RA (1998) Feature detection and identification using a sonar-array. In: *IEEE international conference on robotics and automation (ICRA 1998)*, Leuven, Belgium.

Assad C, Rasnow B and Stoddard PK (1999) Electric organ discharges and electric images during electrolocation. *The Journal of Experimental Biology* 202(10): 1185–1193.

Baffet G, Boyer F and Gossiaux PB (2009) Biomimetic localization using the electrolocation sense of the electric fish. In: *IEEE international conference on robotics and biomimetics (ROBIO 2008)*, Guilin, China.

Bai Y, Snyder J, Silverman Y, et al. (2012) Sensing capacitance of underwater objects in bio-inspired electrosense. In: *IEEE/RSJ international conference on intelligent robots and systems (IROS 2012)*, Vilamoura, Portugal.

Bernhardt J and Pauly H (1973) On the generation of potential differences across the membranes of ellipsoidal cells in an alternating electrical field. *Biophysik* 10(1): 89–98.

Boyer F and Lebastard V (2012) Exploration of objects by an underwater robot with electric sense. In: Lepora NF, Mura A, Krapp HG, et al. (eds) *Biomimetic and Biohybrid Systems*. New York, NY: Springer, pp. 50–61.

Boyer F, Gossiaux PB, Jawad B, et al. (2012) Model for a sensor inspired by electric fish. *IEEE Transactions on Robotics* 28(2): 492–505.

Boyer F, Lebastard V, Chevallereau C, et al. (2013) Underwater reflex navigation in confined environment based on electric sense. *IEEE Transactions on Robotics* 29(4): 945–956.

Calderón AP (2006) On an inverse boundary value problem. *Computational & Applied Mathematics* 25(2–3): 133–138.

Carr CE, Maler L and Sas E (1982) Peripheral organization and central projections of the electrosensory nerves in gymnotiform fish. *Journal of Comparative Neurology* 211(2): 139–153.

Cheney M, Isaacson D and Newell JC (1999) Electrical 1306 impedance tomography. *SIAM Review* 41(1): 85–101.

Church P, McFee JE, Gagnon S, et al. (2006) Electrical impedance tomographic imaging of buried landmines. *IEEE Transactions on Geoscience and Remote Sensing* 44(9): 2407–2420.

Clark DA (2010) Correction of electric and magnetic fields and gradients measured within and around an insulating sensor capsule in seawater. In: *IEEE OCEANS* (2010), Sydney, Australia.

Coiras E, Petillot Y and Lane DM (2007) Multiresolution 3-D reconstruction from side-scan sonar images. *IEEE Transactions on Image Processing* 16(2): 382–390.

Cottis R (2001) Interpretation of electrochemical noise data. *Corrosion* 57(3): 265–285.

Cover TM and Thomas JA (2012) *Elements of Information Theory*. Hoboken, NJ: John Wiley & Sons.

Cowen S, Briest S and Dombrowski J (1997) Underwater docking of autonomous undersea vehicles using optical terminal guidance. In: *MTS/IEEE conference proceedings OCEANS (1997)*, Halifax, Canada.

Culkin F and Smith N (1980) Determination of the concentration of potassium chloride solution having the same electrical conductivity, at 15 °C and infinite frequency, as standard seawater of salinity 35.0000‰ (Chlorinity 19.37394‰). *IEEE Journal of Oceanic Engineering* 5(1): 22–23.

Davis BJ, Gough PT and Hunt BR (2009) Modeling surface multipath effects in synthetic aperture sonar. *IEEE Journal of Oceanic Engineering* 34(3): 239–249.

Dimble KD, Faddy JM and Humbert JS (2014) Electrolocation-based underwater obstacle avoidance using wide-field integration methods. *Bioinspiration & Biomimetics* 9(1): 016012.

Dines KA and Lytle RJ (1981) Analysis of electrical-conductivity imaging. *Geophysics* 46(7): 1025–1036.

Fairfield N, Kantor G, Jonak D, et al. (2010) Autonomous exploration and mapping of flooded sinkholes. *The International Journal of Robotics Research* 29(6): 748–774.

Feder HJS, Leonard JJ and Smith CM (1999) Adaptive mobile robot navigation and mapping. *The International Journal of Robotics Research* 18(7): 650–668.

Fox D, Burgard W and Thrun S (1998) Active Markov localization for mobile robots. *Robotics and Autonomous Systems* 25(3–4): 195–207.

Frieden BR (2004) *Science from Fisher Information: A Unification*. Cambridge: Cambridge University Press.

Friedman JH (1997) On bias, variance, 0/1—Loss, and the curse-of-dimensionality. *Data Mining and Knowledge Discovery* 1(1): 55–77.

Hofmann V, Sanguinetti-Scheck JI, Kunzel S, et al. (2013) Sensory flow shaped by active sensing: Sensorimotor strategies in electric fish. *Journal of Experimental Biology* 216: 2487–2500.

Hollinger GA, Englot B, Hover FS, et al. (2013) Active planning for underwater inspection and the benefit of adaptivity. *The International Journal of Robotics Research* 32(1): 3–18.

Hornegger J and Niemann H (1995) Statistical learning, localization, and identification of objects. In: *Fifth international conference on computer vision (1995)*, Cambridge, MA.

Horowitz P, Hill W and Hayes TC (1989) *The Art of Electronics*, vol. 2. Cambridge: Cambridge University Press.

Horster E and Lienhart R (2006) Approximating optimal visual sensor placement. In: *IEEE international conference on multimedia and expo (ICME 2006)*, Toronto, Canada.

Jackson JD and Jackson JD (1962) *Classical Electrodynamics*, vol. 3. New York, NY: Wiley.

Jaffré FM, Austin TC, Allen BG, et al. (2005) Ultra short baseline acoustic receiver/processor. In: *MTS/IEEE conference proceedings of OCEANS Europe (2005)*, Brest, France.

Jawad B, Gossiaux PB, Boyer F, et al. (2010) Sensor model for the navigation of underwater vehicles by the electric sense. In: *IEEE international conference on robotics and biomimetics (ROBIO 2010)*, Tianjin, China.

Jimenez LO and Landgrebe DA (1998) Supervised classification in high-dimensional space: Geometrical, statistical, and asymptotical properties of multivariate data. *IEEE Transactions on Systems, Man, and Cybernetics, Part C: Applications and Reviews* 28(1): 39–54.

Kinsey JC, Yoerger DR, Jakuba MV, et al. (2011) Assessing the Deepwater Horizon oil spill with the Sentry autonomous underwater vehicle. In: *IEEE/RSJ international conference on intelligent robots and systems (IROS 2011)*, San Francisco, CA.

Krahe R and Fortune ES (2013) Electric fishes: Neural systems, behaviour and evolution. *The Journal of Experimental Biology* 216(13): 2363–2364.

Kreucher C, Kastella K and Hero AO III (2005) Sensor management using an active sensing approach. *Signal Processing* 85(3): 607–624.

Landau L and Lifshitz E (1984) *Electrodynamics of Continuous Media: Volume 8*. Oxford: Pergamon Press.

Land MF (1999) Motion and vision: Why animals move their eyes. *Journal of Comparative Physiology A* 185: 341–352.

Lebastard V, Chevallereau C, Amrouche A, et al. (2010) Underwater robot navigation around a sphere using electrolocation sense and Kalman filter. In: *IEEE/RSJ international conference on intelligent robots and systems (IROS 2010)*, Taipei, Taiwan.

Lebastard V, Chevallereau C, Girin A, et al. (2013) Environment reconstruction and navigation with electric sense based on a Kalman filter. *The International Journal of Robotics Research* 32(2): 172–188.

Legat A and Doleček V (1995) Chaotic analysis of electrochemical noise measured on stainless steel. *Journal of the Electrochemical Society* 142(6): 1851–1858.

Lissmann HW and Machin KE (1958) The mechanism of object location in *Gymnarchus niloticus* and similar fish. *The Journal of Experimental Biology* 35: 451–486.

Li Y and Liu Z (2005) Information entropy-based viewpoint planning for 3-D object reconstruction. *IEEE Transactions on Robotics* 21(3): 324–337.

MacIver MA, Fontaine E and Burdick JW (2004) Designing future underwater vehicles: Principles and mechanisms of the weakly electric fish. *IEEE Journal of Oceanic Engineering* 29(3): 651–659.

MacIver MA, Sharabash NM and Nelson ME (2001) Prey-capture behavior in gymnotid electric fish: Motion analysis and effects of water conductivity. *The Journal of Experimental Biology* 204(3): 543–557.

Miller L, Silverman Y, MacIver M, et al. (2014) Ergodic exploration of distributed information. *Personal communication*.

Nelson ME and MacIver MA (1999) Prey capture in the weakly electric fish *Apteronotus albifrons*: Sensory acquisition strategies and electrosensory consequences. *The Journal of Experimental Biology* 202(10): 1195–1203.

Nelson ME and MacIver MA (2006) Sensory acquisition in active sensing systems. *Journal of Comparative Physiology A* 192(6): 573–586.

Nelson ME, MacIver MA and Coombs S (2002) Modeling electrosensory and mechanosensory images during the predatory behavior of weakly electric fish. *Brain, Behavior and Evolution* 59(4): 199–210.

Neveln ID, Bai Y, Snyder JB, et al. (2013) Biomimetic and bio-inspired robotics in electric fish research. *Journal of Experimental Biology* 216: 2501–2514.

Neveln ID, Miller LM, MacIver MA, et al. (2014) Improving object tracking through distributed exploration of an information map. In: *IEEE/RSJ international conference on intelligent robots and systems (IROS 2014)*, Chicago, IL.

Nguyen N, Wiegand I and Jones DL (2009) Sparse beamforming for active underwater electrolocation. In: *International conference on acoustics speech and signal processing ICASSP*, pp. 2033–2036.

Patterson B, Abraham A, MacIver MA, et al. (2013) Visually guided gradation of prey capture movements in larval zebrafish. *The Journal of Experimental Biology* 16: 3071–3083.

Pinto M, Bellettini A, Wang LS, et al. (2004) A new synthetic aperture sonar design with multipath mitigation. *High Frequency Ocean Acoustics* 728: 489–496.

Rasmussen CE (2006) *Gaussian Processes for Machine Learning*. Cambridge, MA: The MIT Press.

Rasnow B (1996) The effects of simple objects on the electric field of *Apteronotus*. *Journal of Comparative Physiology A* 178(3): 397–411.

Sattar J, Giguère P and Dudek G (2009) Sensor-based behavior control for an autonomous underwater vehicle. *The International Journal of Robotics Research* 28(6): 701–713.

Schmidt M and Lipson H (2009) Distilling free-form natural laws from experimental data. *Science* 324(5923): 81–85.

Sequeira V, Ng K, Wolfart E, et al. (1999) Automated reconstruction of 3D models from real environments. *Journal of Photogrammetry and Remote Sensing* 54(1): 1–22.

Servagent N, Jawad B, Bouvier S, et al. (2013) Electrolocation sensors in conducting water bio-inspired by electric fish. *IEEE Sensors Journal* 13(5): 1865–1882.

Shiau Y and Valentino AR (1981) ELF electric field coupling to dielectric spheroidal models of biological objects. *IEEE Transactions on Biomedical Engineering* 28(6): 429–437.

Shmaliy Y (2006) *Continuous-Time Signals*. Dordrecht, The Netherlands: Springer.

Silverman Y, Miller L, MacIver MA, et al. (2013) Optimal planning for information acquisition. In: *IEEE/RSJ international conference on intelligent robots and systems (IROS 2013)*, Tokyo, Japan, pp. 5974–5980.

Silverman Y, Snyder J, Bai Y, et al. (2012) Location and orientation estimation with an electrosense robot. In: *IEEE/RSJ international conference on intelligent robots and systems (IROS 2012)*, Vilamoura, Portugal.

Singh H, Roman C, Pizarro O, et al. (2007) Towards high-resolution imaging from underwater vehicles. *The International Journal of Robotics Research* 26(1): 55–74.

Smith R, Frost A and Probert P (1999) A sensor system for the navigation of an underwater vehicle. *The International Journal of Robotics Research* 18(7): 697–710.

Snyder JB, Silverman Y, Bai Y, et al. (2012) Underwater object tracking using electrical impedance tomography. In: *IEEE/RSJ international conference on intelligent robots and systems (IROS 2012)*, Vilamoura, Portugal.

Solberg JR, Lynch KM and MacIver MA (2008) Active electrolocation for underwater target localization. *The International Journal of Robotics Research* 27(5): 529–548.

Stamper SA, Roth E, Cowan NJ, et al. (2012) Active sensing via movement shapes spatiotemporal patterns of sensory feedback. *Journal of Experimental Biology* 215: 1567–1574.

Szeliski R and Kang SB (1995) Direct methods for visual scene reconstruction. In: *IEEE workshop on representation of visual scenes (1995)*, Cambridge, MA.

Takeuchi Y, Ohnishi N and Sugie N (1998) Active vision system based on information theory. *Systems and Computers in Japan* 29(11): 31–39.

Tallgren P, Vanhatalo S, Kaila K, et al. (2005) Evaluation of commercially available electrodes and gels for recording of slow EEG potentials. *Clinical Neurophysiology* 116(4): 799–806.

Turner RW, Maler L and Burrows M (1999) Special issue on electroreception and electrocommunication. *The Journal of Experimental Biology* 202(10): 1167–1458.

Valič B, Golzio M, Pavlin M, et al. (2003) Effect of electric field induced transmembrane potential on spheroidal cells: theory and experiment. *European Biophysics Journal* 32(6): 519–528.

Von der Emde G (2006) Non-visual environmental imaging and object detection through active electrolocation in weakly electric fish. *Journal of Comparative Physiology A* 192(6): 601–612.

Von der Emde G and Fetz S (2007) Distance, shape and more: Recognition of object features during active electrolocation in a weakly electric fish. *Journal of Experimental Biology* 210(17): 3082–3095.

Webster SE, Eustice RM, Singh H, et al. (2012) Advances in single-beacon one-way-travel-time acoustic navigation for underwater vehicles. *The International Journal of Robotics Research* 31(8): 935–950.

Weingarten J and Siegwart R (2005) EKF-based 3D SLAM for structured environment reconstruction. In: *IEEE/RSJ international conference on intelligent robots and systems (IROS 2005)*.

Yoerger DR, Jakuba M, Bradley AM, et al. (2007) Techniques for deep sea near bottom survey using an autonomous underwater vehicle. *The International Journal of Robotics Research* 26(1): 41–54.

Yovel Y, Falk B, Moss CF, et al. (2010) Optimal localization by pointing off axis. *Science* 327(5966): 701–704.

Appendix: Index to Multimedia Extensions

Archives of IJRR multimedia extensions published prior to 2014 can be found at http://www.ijrr.org, after 2014 all videos are available on the IJRR YouTube channel at http://www.youtube.com/user/ijrrmultimedia

Extension	Media type	Description
1	Video	How electric images evolve as simple objects vary in position, size, orientation and shape.